Energy & Environmental Science

Accepted Manuscript

This is an *Accepted Manuscript*, which has been through the Royal Society of Chemistry peer review process and has been accepted for publication.

Accepted Manuscripts are published online shortly after acceptance, before technical editing, formatting and proof reading. Using this free service, authors can make their results available to the community, in citable form, before we publish the edited article. We will replace this *Accepted Manuscript* with the edited and formatted *Advance Article* as soon as it is available.

You can find more information about *Accepted Manuscripts* in the Information for Authors.

Please note that technical editing may introduce minor changes to the text and/or graphics, which may alter content. The journal's standard Terms & Conditions and the Ethical guidelines still apply. In no event shall the Royal Society of Chemistry be held responsible for any errors or omissions in this *Accepted Manuscript* or any consequences arising from the use of any information it contains.

ROYAL SOCIETY OF CHEMISTRY

www.rsc.org/ees

Energy & Environmental Science

RSCPublishing

REVIEW

Toward the rational design of non-precious transition metal oxides for oxygen electrocatalysis

Cite this: DOI: 10.1039/x0xx00000x

Wesley T. Hong,[*a] Marcel Risch,[a] Kelsey A. Stoerzinger,[a] Alexis Grimaud,[a‡‖] Jin Suntivich,[b] Yang Shao-Horn[*a]

Received ooth January 2012,
Accepted ooth January 2012

DOI: 10.1039/x0xx00000x

www.rsc.org/

In this Review, we discuss the state-of-the-art understanding of non-precious transition metal oxides that catalyze the oxygen reduction and evolution reactions. Understanding and mastering the kinetics of oxygen electrocatalysis is instrumental to making use of photosynthesis, advancing solar fuels, fuel cells, electrolyzers, and metal-air batteries. We first present key insights, assumptions and limitations of well-known activity descriptors and reaction mechanisms in the past four decades. The turnover frequency of crystalline oxides as promising catalysts is also put into perspective with amorphous oxides and photosystem II. Particular attention is paid to electronic structure parameters that can potentially govern the adsorbate binding strength and thus provide simple rationales and design principles to predict new catalyst chemistries with enhanced activity. We share new perspective synthesizing mechanism and electronic descriptors developed from both molecular orbital and solid state band structure principles. We conclude with an outlook on the opportunities in future research within this rapidly developing field.

Broader Context

The formation of chemical bonds is an energy dense mode of storing energy. In both nature and technology, the electrochemical generation and consumption of fuels is one of the most efficient routes for energy usage. Solar and electrical energy can be stored in chemical bonds by splitting water or metal oxides to produce hydrogen and metal. These compounds can then be oxidized to produce energy when coupled to the reduction of oxygen. However, these device efficiencies are severely limited by the catalysis of oxygen electrochemical processes – namely the oxygen reduction reaction and oxygen evolution reaction, which have slow kinetics. Non-precious transition metal oxides show promise as cost-effective substitutes for noble metals in commercially viable renewable energy storage and conversion devices. Furthermore, this class of materials has benefitted from a wealth of spectroscopic and first-principles studies in the past few decades, providing the frameworks and theories needed to understand the electronic structure and design optimal catalysts. The incredibly diverse range of chemistries and physical properties that can be explored in oxide families afford numerous degrees of freedom for conducting systematic investigations relating intrinsic material properties to catalytic performance. Here, we present background on the fundamental concepts in catalysis for the rational design of transition metal perovskite oxide catalysts for oxygen electrocatalysis and critically examine the current understanding and its impact on future directions of perovskite catalysts.

[a] *Electrochemical Energy Laboratory, Massachusetts Institute of Technology, Cambridge, MA 02139, USA. E-mail: whong@mit.edu, shaohorn@mit.edu*

[b] *Department of Materials Science and Engineering, Cornell University, Ithaca, NY 14850, USA*

‡ Current address: FRE 3677 "Chimie du Solide et Energie," College de France, 75231 Paris Cedex 05, France.

‖ Current address: Reseau sur le Stockage Electrochimique de l'Energie (RS2E), FR CNRS 3459, 80039 Amiens Cedex, France.

† Electronic Supplementary Information (ESI) available: Details of calculations for Fig. 2. See DOI: 10.1039/b000000x/

Introduction

Energy & Environmental Science Accepted Manuscript

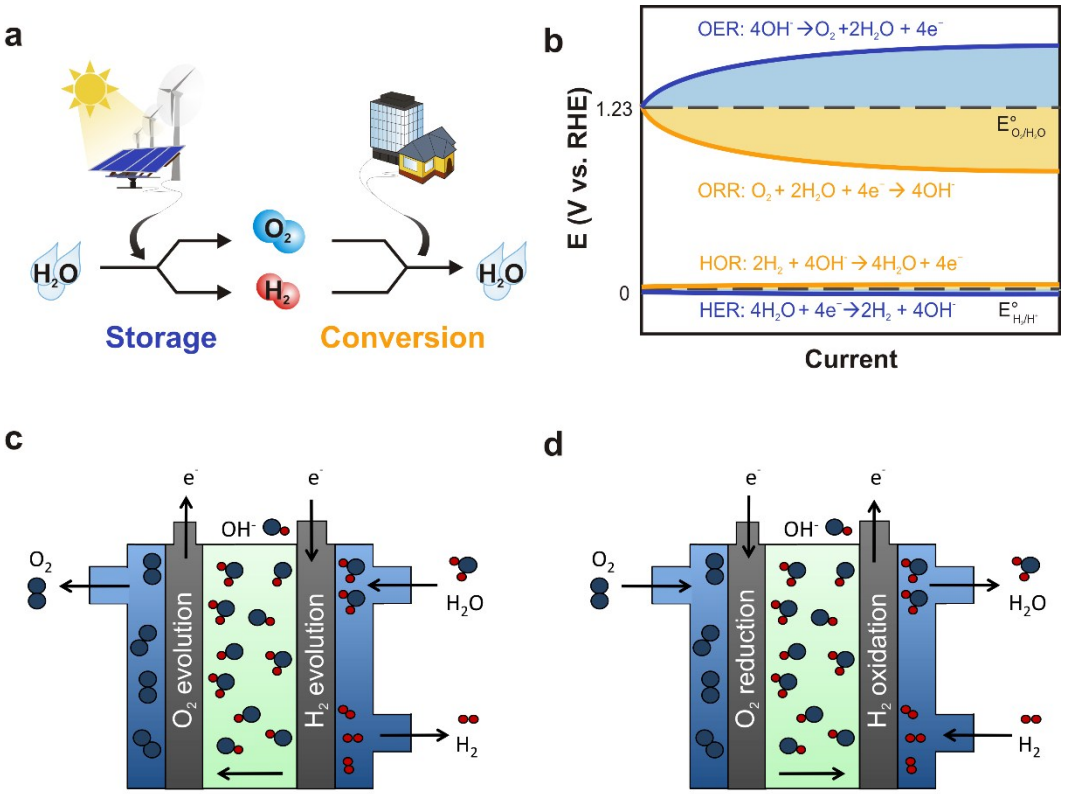

Fig. 1 (a) Hydrogen and oxygen cycle for energy storage and energy conversion. The two half-cell reactions for energy storage by water electrolysis are the oxygen evolution reaction (OER) and hydrogen evolution reaction (HER). For energy conversion, the half-cell reactions are the oxygen reduction reaction (ORR) and the hydrogen oxidation reaction (HOR). (b) Schematic of the overpotentials associated with oxygen electrocatalysis (OER, ORR) and hydrogen electrocatalysis (HER, HOR). Oxygen electrocatalysis severely limits the energy efficiency and rate capability of electrochemical energy devices due to the large overpotential needed to drive the reactions, even when using state-of-the-art catalysts. Reactions shown are formulated for alkaline electrolytes. Schematic illustrations of anion-exchange membrane (c) electrolyzer and (d) fuel cell used with alkaline electrolytes.

Storing electrical energy at scale is arguably the greatest scientific challenge in transitioning from fossil fuels to clean and sustainable energy. Electrochemical reactions are a conceptually simple method to provide and store electrical energy efficiently via chemical bonds.[1] Perhaps most notably, energy can be stored by electrochemically splitting water to form hydrogen and oxygen gas, and their subsequent recombination can provide clean electrical energy where the only by-product is water (**Fig. 1a**). Similarly, energy can be stored by using a metal such as lithium as the energy carrier rather than hydrogen. In this case, reactions involve the formation and reduction of metal oxides instead of water for the energy storage and conversion processes.[2, 3, 4]

However, the kinetic limitations for these oxygen-based electrochemical reactions are often quite large, hampering efficiency in promising technologies such as solar fuels,[5-7] fuel cells,[8, 9] electrolyzers,[5, 10-12] and metal-oxygen batteries.[2, 13-15] For example, the majority of the energy lost in low-temperature hydrogen fuel cells is due to the slow kinetics of the oxygen reduction reaction (ORR, **Fig. 1b**), both in acidic (H^+ proton-exchange membrane) and alkaline (OH^- anion-exchange membrane, **Fig. 1d**) environments.[8, 16-18] Similar losses have also been reported for electrolyzers[5, 19] (**Fig. 1c**) and metal-air batteries[13, 20] due to the poor kinetics of the oxygen oxidation reaction – more commonly referred to as the oxygen evolution reaction (OER). The use of highly active and cost-effective catalysts to promote the oxygen half-reactions plays a pivotal role in realizing these devices for the wide distribution and use of renewable energy.[8, 16, 21]

While oxygen reduction and oxidation (redox) is studied under a number of operating conditions for aqueous,[6, 7, 22] nonaqueous,[2, 3] and solid-state devices,[9, 23] we focus this review on oxygen electrocatalysis in aqueous solutions. In aqueous environments, the oxygen half-cell reactions can be performed in acidic solutions:

$$O_2 + 4H^+ + 4e^- \leftrightarrow 2H_2O,$$

as well as alkaline solutions:

$$O_2 + 2H_2O + 4e^- \leftrightarrow 4OH^-.$$

The standard Nernstian potential for the oxygen half-cell reaction is 1.23 V vs. reversible hydrogen electrode (RHE),[24] which is defined by the hydrogen standard electrode potential for a given pH value. At pH = 0, this potential is referred to as

Energy & Environmental Science Accepted Manuscript

 This journal is © The Royal Society of Chemistry 2012

the standard hydrogen electrode (SHE) scale.[25] The ORR is kinetically favoured below the half-cell potential while the OER is thermodynamically favourable above the potential. However, because the ORR/OER kinetics are very poor, a large deviation from the half-cell potential – which is referred to as the "overpotential" – is needed to yield appreciable current. Understanding the physical origin of the reaction overpotential is a key step toward developing more efficient electrocatalysts for the oxygen half-cell reaction.

To date, the best known catalysts for oxygen electrocatalysis in acidic solutions are Pt-alloy catalysts[26-29] for the ORR (~$50/g)[30] and ruthenium oxides for the OER (~$2.50/g)[30]. However, these catalysts still have overpotentials of ~0.4 V at a practical current density of 1.5 A/cm$^2_{geo.}$.[28, 31] In addition, the scarce crustal abundance of platinum group metals limits their commercial viability.[32] On the other hand, oxygen redox in basic solutions can be catalyzed by metal oxides that contain earth-abundant elements[32] such as non-precious transition metals (e.g. Fe: ~$0.0001/g; Co: ~$0.03/g; Ni: ~$0.02/g)[30] and early rare-earth metals (e.g. La: ~$0.02/g)[30]. The best-known oxide catalysts today include manganese oxides for the ORR and nickel-iron-cobalt oxides for the OER, requiring overpotentials around 0.4 V at 10 mA/cm$^2_{geo.}$.[5, 33]

An alternative measure of the reaction kinetics is the turnover frequency (TOF). The TOF at a given overpotential is typically defined as the number of reaction products generated per active site per unit time. The estimated TOF of common ruthenium and cobalt oxides spans a range of three orders of magnitude (**Fig. 2**).[11, 34-44] Studying differences in the TOF rather than the overpotential allows one to draw comparisons with molecular catalysts and biocatalysts. Most notably, a key oxygen-evolving complex is used in photosystem II, one of the protein complexes involved in photosynthesis.[11] For this oxygen-evolving complex, the estimated TOF is at least one order of magnitude above that of the best oxide catalyst particle, thereby setting a natural benchmark for the OER.[11]

From **Fig. 2**, it is readily apparent that a wide range of oxygen electrocatalytic responses are possible, even for a single transition metal: cobalt oxides alone span nearly three orders of magnitude in TOF. To facilitate the design of new oxide electrocatalysts, relationships can be developed correlating the material's catalytic effects ("activity") to its physical properties, typically referred to as descriptors.[45] For the past 40 years, fundamental understanding of oxide catalysts has been driven by identifying such descriptors that may govern the catalytic activity.

The rational design of oxide electrocatalyst chemistry and nanostructures is therefore one of the central challenges for oxygen electrochemical technologies and the primary focus of this Review. We first discuss key fundamental concepts in oxygen electrocatalysis. We then provide an overview of reported activity trends and descriptors proposed for the ORR/OER on oxides from experiments and density functional theory (DFT) studies by highlighting landmark works in the field. Moreover, we describe the importance of figures of merit normalized to the catalyst surface area, which provide an intrinsic electrocatalytic activity that can be compared across different studies. Combined with the systematic investigation of composition and electronic structure using model oxide families such as the perovskites, trends in the electrocatalytic activity of oxides can be used to identify novel design principles. Finally, we conclude by providing a perspective on open questions on the ORR/OER mechanisms on oxide surfaces and some of the potentially interesting research directions for further improving catalytic activity and obtaining deeper understanding of these reactions at the molecular level.

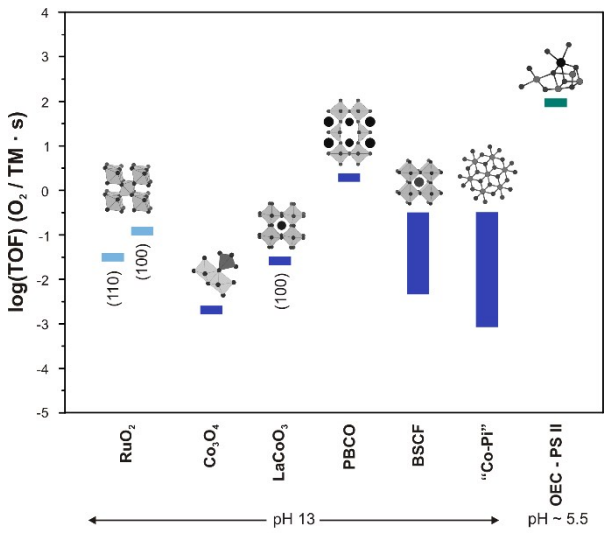

Fig. 2 Turnover frequencies (TOF) of select cobalt oxides (dark blue) compared to thin-film surfaces of rutile RuO_2 (grown on MgO; light blue)[34] and the Mn_4Ca oxygen evolution complex of Photosystem II (OEC – PS II; green)[11] at 0.3 V overpotential. The cobalt oxides (dark blue) are: commercial Co_3O_4 powder (Alfa Aesar),[35] $LaCoO_3$ (001) thin film (grown on Nb:$SrTiO_3$), $PrBaCo_2O_{5+\delta}$ powder (PBCO),[36] $Ba_{0.5}Sr_{0.5}Co_{0.8}Fe_{0.2}O_{3-\delta}$ (BSCF, grown on $La_{0.8}Sr_{0.2}MnO_{3-\delta}$ on $SrTiO_3$),[37] electrodeposited cobalt hydroxide ("Co-Pi"[38]).[39] All oxide measurements were performed in O_2-saturated KOH (0.1 M; pH 13). The TOF of OEC – PS II was calculated for membrane particles (pH ~ 5.5 in the lumen).[11] Representative structural motifs are shown for each catalyst (light grey octahedral or atoms: transition metals; small dark atoms: oxygen; large dark atoms: group II or lanthanides). The upper bound was calculated by dividing the current converted to oxygen flux (O_2/s) for 100% Faradaic efficiency by the number of transition metals on the surface, which was determined using refined lattice parameters and the surface area of the oxide as determined by BET for powders, assuming a (100) surface, and the geometric surface of thin films corrected for roughness. Due to the reported bulk activity of BSCF and "Co-Pi," we give a range for the TOF of these catalysts calculated based on the assumptions that either only atoms on the surface are active (upper bound) or all atoms are active (lower bound). The surface density of "Co-Pi" was estimated from EXAFS data[40, 41] using the method in ref. 42. For "Co-Pi," the number of Co atoms in the bulk was controlled during deposition (25 mC/cm^2 ≈ 250 nmol/cm^2). For BSCF, the number of bulk atoms was calculated using the unit cell volume, film height, and electrode area. The TOF of PS II was estimated as the reciprocal of the total duration for one catalytic turnover (~2.73 ms)[11] divided by 4 Mn atoms. The overpotential of 0.3 V for OEC-PS II was estimated by Dau and Zaharieva[43] as the potential difference between the main oxidant tyrosine (Yz) of 1.2 V vs. NHE and the equilibrium potential of oxygen evolution at pH 5.5 of 0.9 V vs. NHE.[44]

Linear free energy relationships in electrocatalysis

Similar to the study of chemical reactions, classical transition state theory is essential to the understanding of electrochemical

Energy & Environmental Science Accepted Manuscript

reaction rates (**Fig. 3**). In the course of a reaction, the reactants move from an initial state to a final state along a reaction pathway, typically referred to as the reaction coordinate. At a point in the reaction coordinate where the electrochemical free energy must increase for the reaction to proceed ("move uphill"), the reaction encounters an energy barrier referred to as the activation energy ($\Delta G^{\ddagger}$). The transient state that the system passes through at the top of this energy barrier is known as the transition state. If the system initially has insufficient energy to promote the reaction past the transition state, the reaction rate is limited by the energy needed to overcome the barrier. Catalysts promote the reaction kinetics by providing an alternative path with reduced activation energy (**Fig. 3**). More in-depth discussion can be found in previous reviews.[46-48]

Because the transition states are difficult to calculate and measure due to their extremely short lifetimes, the local energy minima on either side of the barrier are typically studied, which may include the initial reactant state, the final product state, or states generally referred to as intermediates (**Fig. 3**). These states are easier to both measure and compute, and can be related to the transition state by linear free energy relationships (LFERs). LFERs are a phenomenological model used to describe the linear behavior that may exist between the logarithm of the reaction rates and equilibrium constants for a series of reactions:[49-51] $\ln k = a \ln K + b$, where k denotes the kinetic rate constant, K denotes the thermodynamic equilibrium constant, and a and b are constants. These can be equivalently written in terms of the activation free energies ($k \propto \exp\left(\frac{-\Delta G^{\ddagger}}{RT}\right)$) and equilibrium intermediate free energies ($K \propto \exp\left(\frac{-\Delta G^{\circ}}{RT}\right)$). The fundamental implication of an LFER is that as an intrinsic variable (e.g. electric potential ϕ, chemical potential μ, temperature T, pressure p, etc.) is tuned, the change in activation energy scales with the change in intermediate energy.[52] Developing correlations between reaction rates and these independent variables allows researchers to identify parameters that govern the kinetics. For instance, the Tafel relation is a notable LFER in electrocatalysis in which the kinetics of an electrochemical reaction (i.e. current density, i) can be related to the overpotential, η ($\ln i \propto \eta$).[51] The Tafel relation thus describes the potential dependence of the reaction rate-determining step(s). Similarly, the oxygen surface exchange coefficient (rate constant) for solid oxide fuel cell cathodes can be correlated with the partial pressure of oxygen ($\ln k \propto \ln p_{O_2}$).[23]

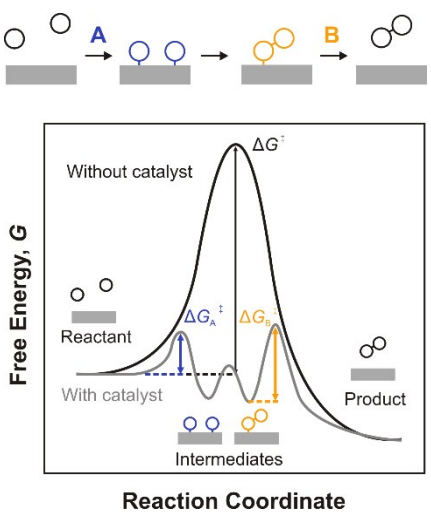

Fig. 3 Schematic illustrations of a prototypical reaction mechanism, transition state theory, and its associated linear free energy relationships. Potential energy landscape along a chemical reaction coordinate and the reduction of the effective reaction barrier due to a catalyst. Illustration of the reaction barriers without a catalyst ($\Delta G^{\ddagger}$) and with a catalyst ($\Delta G_A^{\ddagger}$, $\Delta G_B^{\ddagger}$). Activation barriers for the reaction are effectively reduced by the presence of stable intermediate states on a catalyst surface.

Recent computational studies have also employed LFERs to predict catalytic activity trends of reactions on metal surfaces.[53, 54] These studies found linear relations between the transition state activation energy and the change in enthalpy of the reaction step – a special case of LFERs in the limit of an isentropic reaction series (i.e. the change in entropy of the reaction is similar across the series) typically referred to as the Brønsted–Evans–Polanyi (BEP) relation.[50, 51] Using the LFER that exists between the electrochemical free energy of reaction intermediates and the reaction rate, a thermodynamic electrochemical overpotential can be defined as the potential that must be applied such that the intermediate free energies for all steps along the reaction coordinate are spontaneous (i.e. energetically downhill).[55] The step with the largest barrier determines the thermodynamic overpotential and is referred to as the potential-determining step.[56]

First we show and discuss reported DFT results of thermodynamic electrochemical overpotentials for the ORR and OER on metal surfaces,[55] where similar elementary reaction steps have been used to study ORR and OER kinetics on oxide surfaces. Here, four proton-coupled electron transfer steps[57] were assumed on a single metal site, and oxygen recombination was excluded due to its large activation barrier on metal surfaces with low oxygen coverage.[58] In an acidic environment, the four reaction steps of the ORR/OER can be written as:

$$O_2 + 4H^+ + 4\,e^- \leftrightarrow OOH^* + 3H^+ + 3e^-$$
$$OOH^* + 3H^+ + 3e^- \leftrightarrow O^* + H_2O + 2H^+ + 2e^-$$
$$O^* + H_2O + 2H^+ + 2e^- \leftrightarrow OH^* + H_2O + H^+ + e^-$$
$$OH^* + H_2O + H^+ + e^- \leftrightarrow 2H_2O$$

where * denotes a surface site. Equivalently the reactions can be written in terms of alkaline environments:

$$O_2 + 2H_2O + 4\,e^- \leftrightarrow OOH^* + H_2O + OH^- + 3e^-$$
$$OOH^* + H_2O + OH^- + 3e^- \leftrightarrow O^* + H_2O + 2OH^- + 2e^-$$

Energy & Environmental Science Accepted Manuscript

This journal is © The Royal Society of Chemistry 2012

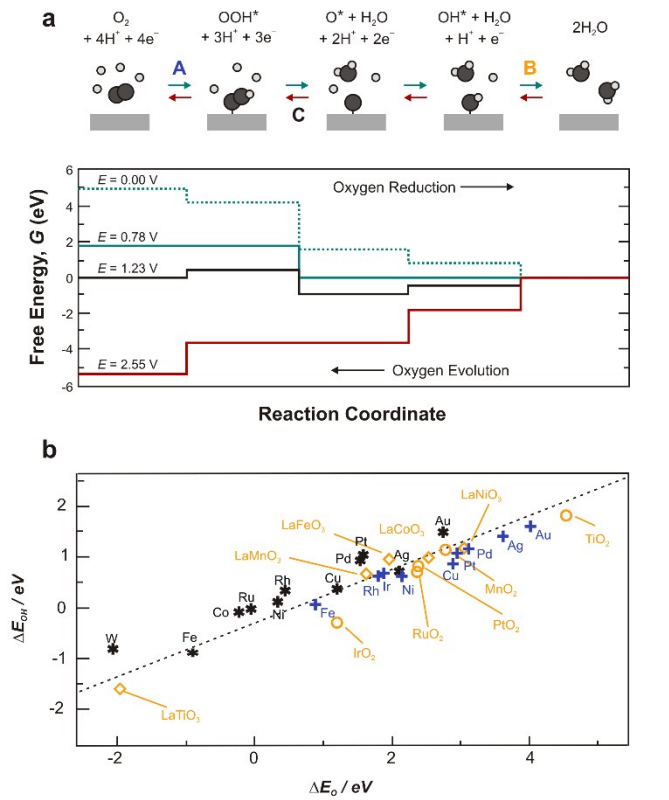

Fig. 4 (a) A schematic of a four-step, four-electron ORR and OER mechanism on a metal surface, e.g. Pt (111).[55] A and B denote the typical ORR rate-determining steps observed on different metal surfaces in DFT calculations. The computed potential energy surface for the ORR (left to right) and the OER (right to left) at different potentials on a platinum surface is shown below. At potentials (E vs. RHE) below E = 0.78 V vs. SHE, all steps in the ORR are spontaneous. For potentials beyond E = 2.55 V vs. SHE, all OER steps become spontaneous (assuming the OER mechanism is the reverse of the proposed ORR mechanism). Figure adapted from ref. 55 with permission by Elsevier. (b) Adsorption energies of OH* plotted against the adsorption energy of O* on surfaces of metals in an unconstrained generalized gradient approximation (GGA) type DFT calculation (black asterisk) and forced on top of a metal site (blue cross; oxide-like configuration), perovskite oxides (yellow diamonds) and rutile oxides (yellow circles). The dashed line indicates the scaling relation between ΔE_{OH} and ΔE_O. Figure adapted from ref. 59 with permission from Wiley and Sons.

$$O^* + H_2O + 2OH^- + 2e^- \leftrightarrow OH^* + 3OH^- + e^-$$

$$OH^* + 3OH^- + e^- \leftrightarrow 4OH^-$$

Note that the reaction intermediates are the same for the ORR/OER in acid and base (OOH*, O*, and OH*); here we use the acid notation for discussion. The number of electrons in each intermediate state influences the potential dependence of the state. The adsorption free energies of the ORR/OER intermediates at select potentials (E vs. RHE) on platinum (111) are shown in **Fig. 4a**.[55] At the equilibrium voltage of 1.23 V, the formation of OOH* from O_2 (step A in **Fig. 4a)** is thermodynamically uphill for the ORR while the formation of OOH* from O* (Step C in **Fig. 4a**) is uphill for the OER. Applying a voltage to move the potential away from 1.23 V is therefore necessary for all reaction steps in this mechanism to proceed spontaneously for both the ORR and OER, yielding non-zero thermodynamic overpotentials. On other metal surfaces, the protonation of OH* on the surface (Step B in **Fig. 4a**) was found to be rate-limiting.

The free energy landscape depicted in **Fig. 4a** illustrates that the optimal catalyst should have no difference in the intermediate free energies at the equilibrium voltage. Under these conditions, the transitions from one intermediate state to another would be spontaneous for both the ORR and the OER, and the catalyst would theoretically achieve the equilibrium voltage of 1.23 V. However, the energies of these intermediates are highly correlated, and scaling between their adsorption energies causes them to move in a concerted fashion for both metal and oxide surfaces (**Fig. 4b**).[59] These scaling relations are fundamental properties of the reaction intermediates and are independent of the electrocatalytic surface.

The scaling relations lead to some important consequences on catalyst design. First, the scaling relation between the adsorption energies (ΔE_X, X = OOH*, OH*, O*) of OOH* and OH* suggests that the most active catalysts have a non-zero overpotential for this four-step mechanism.[56, 60] Rossmeisl, [55, 61] Koper[56] and their co-workers have shown that the intermediate adsorption energies on two-dimensional surfaces can never accommodate this condition because ΔE_{OOH^*} and ΔE_{OH^*} have a 1:1 scaling with a ~3.2-3.4 eV offset (**Fig. 5a**),[60] which differs from the ideal value of 2.46 eV.[11, 56, 62] In contrast, ΔE_{O^*} has a 2:1 scaling with ΔE_{OH^*} and ΔE_{OOH^*} due to the double bond formed with the O* intermediate.[55] Second, the collinearity of the intermediate energies defines the difference between the free energies $\Delta E_{O^*} - \Delta E_{OH^*}$ as a universal descriptor of the OER. Utilizing the same proposed four-step, one-electron transfer model of the ORR/OER as on metal catalysts[55], Man and co-workers have reported the adsorption free energies of reaction intermediates on rutile and perovskite oxides and their thermodynamic overpotentials for the ORR/OER.[60] When the computed thermodynamic overpotentials are plotted against this descriptor, two distinct lines with inversely related slopes are obtained (**Fig. 5b**).[60] This behavior is typically referred to as a volcano relation, where the two different slopes are indicative of different rate-determining steps for the same mechanism. The adsorbates bind to surfaces on the left-hand branch too strongly and bind to the right-hand branch too strongly. This behavior in which the optimal catalyst binds neither too strongly nor too weakly is typically referred to as the Sabatier principle. For clarity in this Review, all figures place the strong-binding branch of volcano relations on the left-hand side and the weak-binding branch on the right-hand side.

While these scaling relations provide a simple, physically intuitive picture of catalyst design, it is important to recognize their limitations. While the predicted trend provides insight into understanding the difference in catalytic activity across chemistries, these relations are only well defined for surfaces that follow the same reaction mechanism; if the reaction mechanism differs among the studied catalysts, the scaling relations change and the simple picture of the volcano relation breaks down. For example, Vojvodic et al. have performed

Energy & Environmental Science Accepted Manuscript

calculations illustrating that the BEP relation for O_2 dissociation on early transition metal perovskites can differ from that of late transition metal perovskites due to different dissociation mechanisms.[63] The above example of the ORR/OER assumes a four-step reaction in which proton transfer is coupled to electron transfer (e.g. proton-coupled electron transfer). We will discuss other mechanisms that have been proposed on oxide surfaces moving beyond this assumption later in this Review.

Activity descriptors and mechanisms proposed for oxygen electrocatalysis

Activity descriptors on metal surfaces

Although these computed activity trends provide a framework to rationalize the importance of metal-oxygen bond strength on the ORR/OER activity, it is not straightforward to predict new catalysts due to the difficulties in experimentally measuring and controlling adsorbate binding strength on surfaces. Significant efforts have been devoted to identifying surface electronic structure characteristics that scale with the binding of oxygen on metal and oxide surfaces,[45, 53, 64-67] which can be used to influence catalytic activity and design new catalyst chemistries.

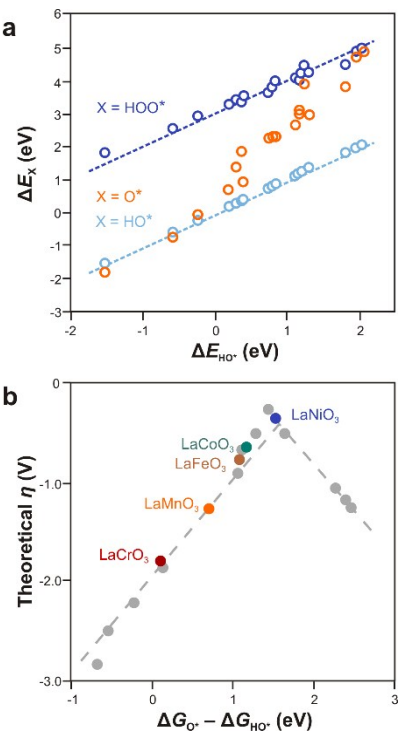

Fig. 5 Generalized gradient approximation (GGA) type DFT calculations of oxygen adsorbates on various perovskite surfaces. (a) Linear scaling relationships between HOO*, O*, and HO* intermediate adsorbates on various perovskite surfaces. The offset between HOO* and HO* intermediates (dashed lines) is +3.2 eV. The Gibbs free energy of adsorption (ΔG) was determined from the internal free energy (ΔE) assuming a constant change in entropy. The data is tabulated in ref. 60. (b) Volcano relation obtained from DFT calculated theoretical overpotentials (closed circles) for the OER on various perovskite surfaces using the difference in binding strength of the O* and HO* intermediates as an activity descriptor. Figure adapted from ref. 60 with permission from Wiley and Sons.

One of the landmark contributions in the development of catalytic activity descriptors is the relationship between the oxygen chemisorption strength on a metal surface and metal electronic structure through the position of the metal's *d*-band center relative to its Fermi level.[53, 64] When the adsorbate binds to the catalyst surface, the adsorbate electrons interact with the metal valence *s*, *p*, and *d* bands to form bonds. To first approximation, the localized metal *d* states govern the bond strength because the *s* and *p* band energies do not change significantly when forming the adsorbate-metal bond. As the *d*-band center shifts toward the Fermi level, the fraction of unoccupied antibonding states formed above the Fermi level increases, increasing the chemical bond strength with the adsorbate.[68] DFT results showed a linear relationship between the *d*-band center and the strength of the metal-oxygen bond on transition metal surfaces. These computational findings were later supported by ultraviolet photoemission spectroscopy (UPS) measurements of the *d*-band center for Pt_3M alloys (M = Ti, V, Cr, Mn, Fe, Co, Ni),[69] although limitations in its applicability for pure transition metals have been discussed elsewhere.[70-72] These realizations have been instrumental in guiding intense scientific research on platinum-alloy catalysts in the past decade.[73-77] One significant work to note is that the *d*-band center of Pt_3M alloys scales with the ORR activity in a volcano trend,[73, 75, 78] which can be used to guide the design and development of new catalyst chemistry.[73, 75, 79]

However, there are several limitations to using precious metal catalysts for oxygen electrochemistry. First, precious metals operate poorly as OER catalysts[80, 81] due to the large overpotential needed to form an oxide layer on the surface before the reaction proceeds.[55, 82, 83] Consequently, comparison between the DFT-computed[55] and experimentally measured OER trends on metal surfaces is not straightforward as the reaction takes place on an oxidized surface. In addition, dissolution of the catalyst surface during the ORR presents major challenges for long-term stability.[84, 85] Exploring oxides for catalysis is a promising direction due to their theoretical stability under both ORR and OER conditions, but this necessitates the development of new descriptors for engineering their catalytic activity.[86, 87]

Traditional activity descriptors on oxide surfaces

The pioneering work of Beer introduced conductive oxide electrodes in oxygen electrocatalysis and rapidly drove the search for cheap and efficient oxide catalysts in industrial settings.[19, 88] These were first referred to as dimensionally stable anodes (DSA) and were poorly understood until a more comprehensive understanding of oxide electronic properties was developed in the 1980s and 1990s.[89-92] Most significantly, the many variables that were observed to influence the DSA's OER electrocatalytic properties instigated considerable interest in developing property-activity correlations that could rationalize modifications to performance.[88] Here we discuss traditional activity descriptors proposed for oxide surfaces that have since developed from the early days of the DSA. We

Energy & Environmental Science Accepted Manuscript

 This journal is © The Royal Society of Chemistry 2012

specifically focus on descriptors for the OER, as the ORR was traditionally studied for metal surfaces.

Tseung and Jasem (1977)[83] were among the first to propose criteria for oxide semiconductor OER anodes. They reasoned that the most promising oxide candidates should have a transition metal redox couple at potentials below the theoretical oxygen electrode in order to form more active higher oxidation state metal sites on the surface. In addition, good electrical conductivity, and high ORR activity were also believed to play important roles in determining highly active OER catalysts. Based on these criteria, they successfully identified RuO_2 and $NiCo_2O_4$ as some of the best oxide electrocatalysts at the time.

In the following years (1980-1984), Trasatti[65, 93] expanded upon these criteria and published a series of works on the OER on rutile, spinel, and perovskite oxides. He identified the first semiquantitative property-activity relationships for oxide OER electrocatalysts, which established the practice of predictive reactivity scales that has largely shaped the field today. In particular, Trasatti focused on oxide properties that reflected the nature of the metal-oxygen bond strength, inspired by the work by Rüetschi and Delahay on metal catalysts.[94] Most notably, the enthalpy of transition from a lower to a higher oxidation state for binary oxides resulted in a volcano relation when plotted against the OER overpotential (**Fig. 6a**).[65] This relation was the first experimental manifestation of the Sabatier principle for the OER: oxides which are oxidized with difficulty are poor catalysts due to their weak affinity for oxygen, and conversely, oxides which are oxidized readily are also poor catalysts because their affinity for oxygen is too strong. In addition to the oxidation enthalpy, Trasatti also reported several lesser-cited property-activity relationships, including the pH of zero charge (pH_{pzc}) and gas-phase isotopic oxygen exchange kinetics.[93]

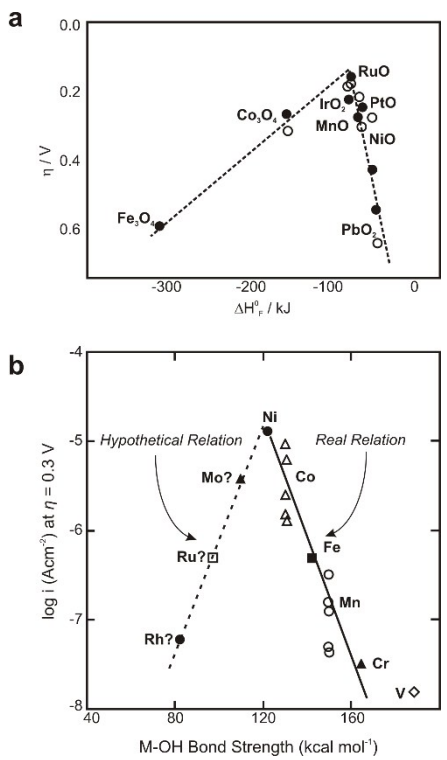

Fig. 6 Early volcano trends of the OER. (a) Overpotential of binary oxides reported by Trasatti as function of the enthalpy of transition from a lower to a higher oxidation state. Measurements in alkaline are shown as open symbols and measurements in acid as filled symbols. Reproduced from ref. 65 with permission by Elsevier. (b) Measured current at 0.3 V overpotential reported by Bockris and Otagawa as function of calculated M-OH bond strength for pellets of first-row transition metal perovskites (transition metal in graph) and extrapolation of the weak binding side using second-row transition metals. Reproduced from ref. 66 with permission by the Electrochemical Society.

Important to note is that at this point in time, these correlations were developed without any assertion of the mechanism occurring on different oxide surfaces (Trasatti explicitly cautioned that "no special attention [had] been paid to build up a mechanistically homogeneous plot"[65]). Rather, the point of these relations were to identify properties that could function as predictive identifiers with simple physical rationale. Deeper investigations of the fundamental reaction mechanisms on these surfaces became the subject of many studies in the following decade.

Chiefly among these, Bockris and Otagawa (1983, 1984)[66, 95] performed a systematic investigation of the perovskite oxide family to attempt to elucidate the mechanism and rationalize the success and failure of specific property-activity relationships. In their work, they found an inverse linear dependence of the current density at constant overpotential on the enthalpy of $M(OH)_3$ hydroxide formation for eighteen different perovskite oxides (**Fig. 6b**).[66] They concluded that a common rate-determining step must be shared among these oxides – the desorption of OH* intermediates.

These works became the foundation of oxide electrocatalyst design for the subsequent 20 years, during which the majority of research focused on understanding reaction pathways and active site design for specific catalysts.

Proposed reaction mechanisms on oxide surfaces

In **Fig. 7**, we illustrate some of the mechanisms proposed for oxide surfaces that were rationalized from different approaches. The mechanisms have primarily been proposed for the OER in alkaline solutions, although the reverse cycle has also been suggested for the ORR for several of the mechanisms.

Many of the mechanistic insights for the ORR were originally developed for noble metal surfaces. Earlier, we discussed the four-step ORR/OER reaction mechanism that was determined from the extensive computational work on metals, which involves only proton-coupled electron transfers. This mechanism was extended to oxide surfaces by Man et al.[60] to rationalize the trends in catalytic activity of perovskites and rutile oxides for the OER (**Fig. 7a**). It is sometimes referred to as an acid-base mechanism[96, 97] because it proceeds through a series of acid-base steps, in which OH, an oxygen nucleophile (Lewis acid) attacks a metal-bound, electrophilic oxygen surface species (Lewis base). An identical reaction mechanism was proposed by Goodenough et al. for the ORR on pyrochlore and rutile oxides (**Fig. 7b**).[98] Computational work on the OER

Energy & Environmental Science Accepted Manuscript

by van Voorhis and co-workers found that this reaction mechanism is also the most favorable in dimeric metal "oxide" molecules with early transition metal ions (**Fig. 7c**).[96] Note that Mechanism **7a** involves a step with a bare catalyst surface, while Mechanisms **7b** and **7c** do not. Metal oxides can adsorb species from solution (e.g. H*, OH*, O*, etc.) depending on the surface's pH of zero charge (pH_{pzc}).[99, 100] At pH values higher than the pH_{pzc}, negatively charged species accumulate on the surface (e.g. OH*, OOH*, O*, etc.). ORR/OER activities of oxides are typically performed at pH values of 13-14, which are much higher than the pzc of most oxides (~7-11 for binary oxides[101] and perovskites[66]). Therefore, oxide surfaces are expected to accumulate negatively charged adsorbates such as OH^- in alkaline solution.[102]

In the above mechanism, the entire reaction proceeds on a single metal site. Two-site mechanisms involving chemical steps – such as the recombination of oxygen adsorbates to form O_2 or the dissociation of water – are not considered as viable reaction pathways. Recent work by Halck et al.[103] suggested that introducing a two-site mechanism can alter the scaling relations between intermediates to reduce the overpotential. Calculations by van Voorhis and co-workers found that such pathways are competitive in dimeric molecules with late transition metals (e.g. Co, Ni, Cu).[96] A two-site reaction mechanism was proposed previously for RuO_2 surfaces by Trasatti and co-workers[104] in acidic solution via the recombination of surface oxygen species (reformulated for alkaline in **Fig. 7d**). This mechanism proceeds similarly to the acid-base mechanism, but the evolution of oxygen does not occur through the potentially rate-limiting OOH* species. While such reaction mechanisms have been shown to have large activation barriers on noble metal surfaces,[58] the presence of loosely bound lattice oxygen atoms in oxide surface terminations have been observed to facilitate such reaction steps in the OER by ^{18}O isotope studies on RuO_2[105] and $NiCo_2O_4$[106]. More distinct two-site mechanisms have also been proposed for electrodeposited oxides[107] and the oxygen evolving complex of PS II[108, 109] (Mechanisms **Fig. 7e** and **7f** respectively). Although these catalysts can differ strongly from crystalline solids, these mechanisms illustrate other pathways that may be possible depending upon the coordination of the transition metal.

The diversity in reaction mechanisms that have been proposed highlights the complexity of assigning a reaction mechanism to oxygen electrochemical reactions on oxide surfaces and PS II, especially for different chemistries. The mechanisms described above involve several types of reaction intermediates, and there has been no method for unambiguously distinguishing reaction intermediates on oxide surfaces to date. Moreover, because many of the proposed mechanisms share

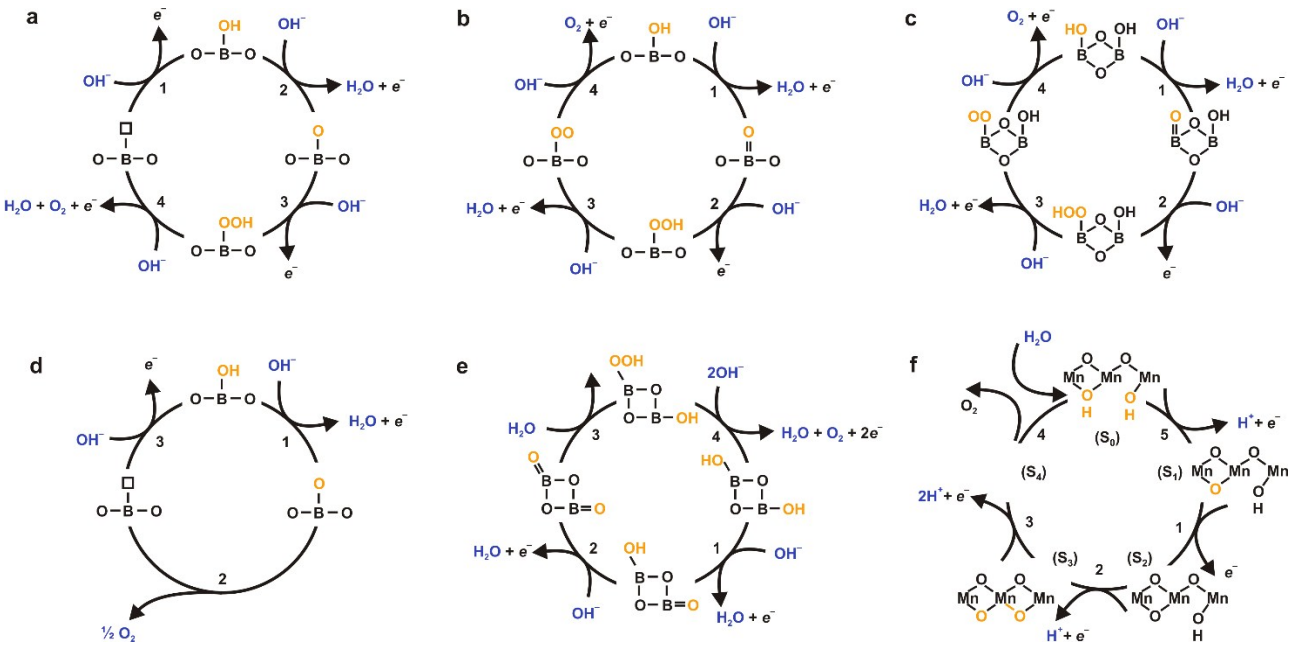

Fig. 7 OER mechanisms proposed for crystalline oxide surfaces, amorphous oxide surfaces, molecules and the oxygen evolution complex of photosystem II (OEC-PS II). Except for photosystem II (being in a mildly acidic environment), all catalytic cycles are formulated for alkaline electrolytes. (a) Four-step reaction mechanism proposed by Rossmeisl and co-workers for the OER on noble metal catalyst surfaces,[55] and later applied to oxide surfaces.[60] (b) Four-step reaction mechanism proposed by Goodenough et al. for the OER on perovskite surfaces.[98] (c) Acid-base mechanism proposed for dimeric molecules.[96] (d). Reaction mechanism proposed by Trasatti and co-workers involving recombination of oxygen atoms to produce O_2.[104] (e) Reaction mechanism proposed by Gerken et al. for electrodeposited oxides in buffered conditions (pH 3.5 to 14).[107] (f) Structural changes of the OEC – PS II proposed by Dau, Haumann and coworkers based on X-ray absorption spectroscopy.[108] Three of the four manganese ions are sufficient to show the catalytic cycle, which proceeds through states S_0 to S_4 by light flashes.[109] In all panels, orange denotes species on the catalyst surface and blue denotes species in solution. The transitions are labeled starting from the resting state of the catalyst, i.e. the state in equilibrium with the surroundings in absence of external stimuli (voltage or light).

Energy & Environmental Science Accepted Manuscript

 This journal is © The Royal Society of Chemistry 2012

similar intermediates, time-resolved techniques must be further developed to verify the various steps in the reaction pathway. Additional treatments of possible reaction mechanisms and their electrochemical responses can be found in the literature.[95, 110] As we alluded to earlier, further insights for understanding chemistry-dependent differences in mechanisms may also be drawn from comparisons of the mechanisms on oxide surfaces discussed here with more detailed investigations on transition metal complexes and the OEC; we direct interested readers to other reviews on the ORR[111] and OER[112] for these systems.

Recent developments on the estimation of oxide intrinsic activity for oxygen electrocatalysis

Many of the studies that established the ground work of oxygen electrocatalysis on oxide surfaces in the 1970s and 1980s were performed on ceramic pellets. The use of pressed discs presents some fundamental challenges. First, it makes it difficult to deconvolute true electrocatalytic effects from electron transport effects in semiconducting or insulating oxide catalysts. Second, it requires that current densities be normalized by the geometric surface area of the disc. Ideally the current density should be determined by the electrochemically active surface area, which may be influenced by roughness or porosity of the sample. Although general chemical trends can be obtained provided the sample roughness is comparable for different chemistries, deeper kinetic insights – such as the Tafel slope or other LFER behavior – cannot be extracted accurately. In the following section, we describe some technical aspects of electrochemical measurements that should be considered for more accurately determining a catalyst's intrinsic activity.

The three-electrode electrochemical cell

Activities of oxides for oxygen electrocatalysis can be obtained using cyclic voltammetry (CV) or galvanostatic measurements in a three-electrode cell (**Fig. 8**), which consists of a working electrode, a counter (or auxiliary) electrode, and a reference electrode. Additionally, ion-blocking membranes and separate electrode compartments connected by salt bridges[113] are common to avoid unwanted reactions on the electrodes.[114] For oxides in powder form, a catalyst layer that consists of oxide powder, Nafion® and carbon[115], can be deposited on conducting substrates that exhibit low OER/ORR activities, such as glassy carbon electrodes (GCE).[116] Together, the glassy carbon substrate and catalyst serve as the working electrode. For oxides grown directly or electrochemically deposited on a conductive substrate (e.g. Nb:$SrTiO_3$),[117] the sample can be used directly as the working electrode. Many different reference electrodes can be used; one commonly used is the calomel electrode, which employs the reversible redox between $2Hg + 2\ Cl \leftrightarrow Hg_2Cl_2$ in saturated KCl. An environmentally more benign alternative is the silver chloride reference electrode: $Ag + Cl \leftrightarrow AgCl$. Caution should be exercised when using these electrodes in a one-compartment cell, as chlorine can leach from the reference electrode and diffuse to the working electrode. If the interference of chloride ions on the activity is of particular concern, activity measurements can be repeated using reference electrode chemistries based on mercury oxide, mercury sulfate, or silver sulfate. Alternatively, a more elaborate cell design with membranes and/or separated compartments can be used. For the counter electrode, it is important to pick one with a chemistry and surface area such that the reaction does not limit the oxygen half-cell reaction at the working electrode. Platinum wires are typically used as the counter electrode due to their chemical stability and high activities for the hydrogen half-cell reaction, i.e. the hydrogen evolution reaction (HER) and the hydrogen oxidation reaction (HOR).

The cell potential can be controlled or measured across the working and reference electrodes with negligible current flow, while the cell current can be measured or controlled across the working and counter electrodes. For OER/ORR, it is useful to convert the potentials measured to the thermodynamically relevant scale of RHE. Experimentally, the reference electrode can be calibrated against the RHE scale by measuring HER/HOR kinetics on a Pt working electrode in a hydrogen-saturated electrolyte (1 bar hydrogen pressure) under the same electrolyte concentration, temperature, and pH used for ORR/OER activity measurements. For vanishing current, these reactions are in equilibrium, which defines zero on the RHE

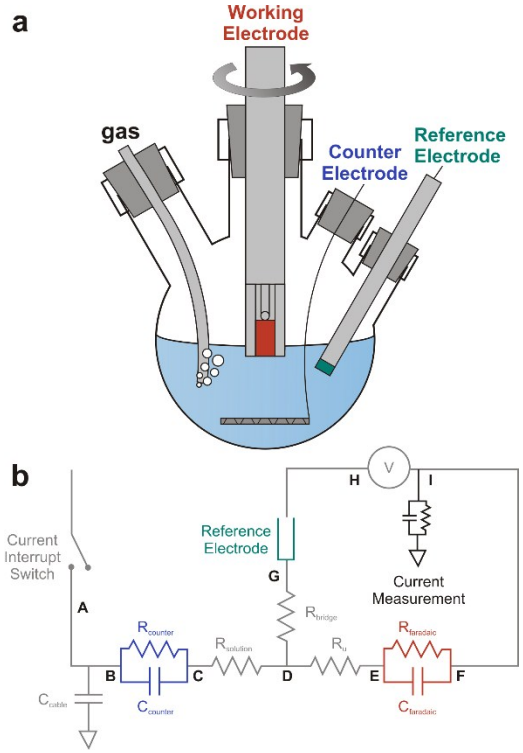

Fig. 8 Schematic of a three-electrode electrochemical cell. (a) Experimental setup for the three-electrode cell. (b) Circuit of a typical three-electrode cell. In these cells, the potential is measured or controlled between the working and reference electrodes (H), while the current is measured or controlled between the working and counter electrodes (I). The working electrode can be rotated to avoid limitation by transport of the analyte.

Energy & Environmental Science Accepted Manuscript

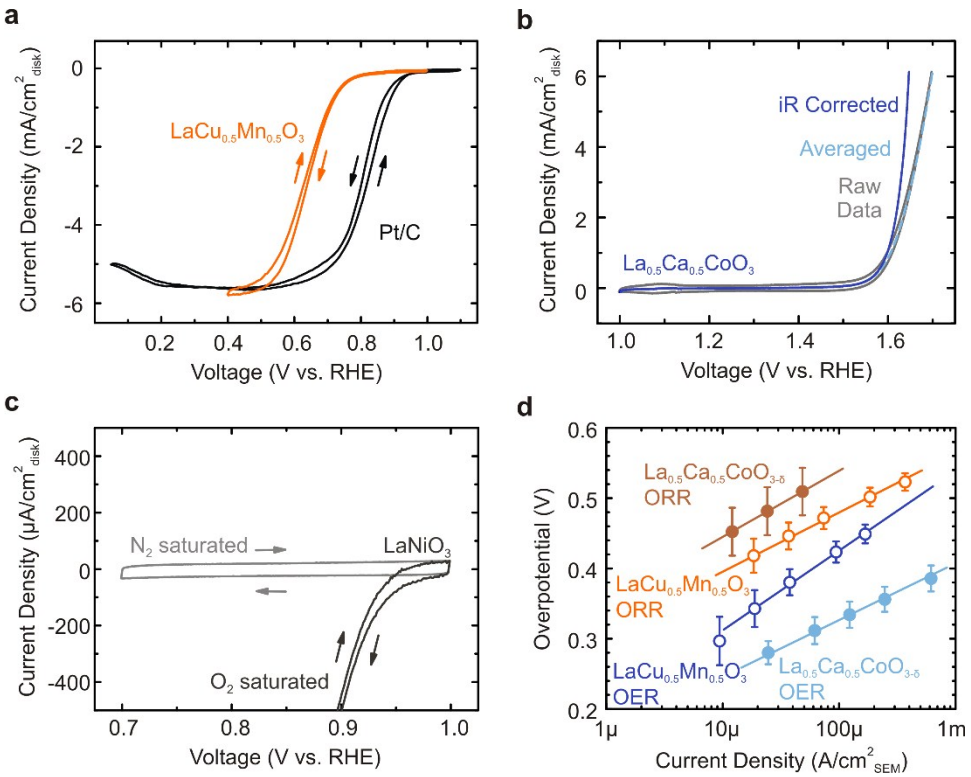

Fig. 9 Examples of CV corrections for ink-casted electrodes in 0.1 M KOH (pH 13) and activity comparison of selected perovskite oxides. (a) Comparison between the ORR activity of $LaCu_{0.5}Mn_{0.5}O_3$ and the benchmark Pt/C (46 wt % Pt on high surface area carbon, Tanaka Kikinzoku Kogyo, Japan). Arrows indicate sweep direction; the backwards scan is used to obtain ORR activities. Reproduced from ref. 116 with permission from the Electrochemical Society. (b) Ohmic and capacitive corrections of the as-measured OER activity of $La_{0.5}Ca_{0.5}CoO_{3-\delta}$. The raw data (grey) is corrected for capacitance by taking the average of the forward and backward scans (light blue). The voltage, E, is corrected for Ohmic resistance (dark blue) using $E_{corrected} = E_{raw} - iR$, where i is the current and R is the cell resistance (typically ~ 50 Ω with our setup). Reproduced from ref. 67 with permission from AAAS. (c) Cyclic voltammograms of $LaNiO_3$ in N_2-saturated KOH at 0 rpm and in O_2-saturated KOH at 1600 rpm. Arrows indicate sweep direction. Reproduced from ref. 116 with permission from the Electrochemical Society.(d) Tafel plots comparing the ORR (yellow; data from ref. 164) and OER (blue; data from ref. 67) activities of $La_{0.5}Ca_{0.5}CoO_{3-\delta}$ (light solid circles) and $LaCu_{0.5}Mn_{0.5}O_3$ (dark open circles). All measurements were performed in a three-electrode cell with an ink-casted glassy carbon disk rotating at 1600 rpm and sweep speed was 10 mV/s unless otherwise noted. The catalyst ink was prepared by mixing oxide, acetylene carbon and K-exchanged Nafion with weight ratio 1:5:5. The current is normalized by the oxide surface area as determined by scanning electron microscopy analysis.

scale.

In the measurement of the ORR activity, the use of a rotating disk electrode (RDE) can mitigate mass-transport losses, allowing for more reliable measurement of the reaction kinetics.[118] The influence of mass transport on the ORR kinetics at high overpotentials while rotating result in a well-defined mass-transport-limiting current (**Fig. 9a**), which can be tuned by the rotation speed based on the Levich equation.[119] In addition, the electrolyte should be pre-saturated by bubbling oxygen for an extended time, and oxygen transport to the electrode can be optimized by the flow rate of oxygen and/or stirring the solution.[120]

Corrections to extract the ORR/OER kinetic current

The measured potentials should be corrected for Ohmic resistances, for which the greatest contribution is usually the uncompensated resistance of ionic conduction in the electrolyte between the working and reference electrodes. This correction is particularly important for measurements made in conventional three-electrode cells, which have a large distance between the working and counter electrodes (e.g. 2 cm for PINE cells). The true potential of the working electrode is given by:

$$E_{true} = E_{measured} - iR_u$$

where i is the cell current and R_u is the uncompensated resistance (**Fig. 9b**, dark blue line). The uncompensated resistance can be determined by impedance spectroscopy or the current interrupt method.[121] Although it is possible to dynamically compensate for the Ohmic drop in modern potentiostats, the use is not advisable because the circuit consisting of the potentiostat and the electrochemical cell could drift into the resonance condition by subtle changes of the electrolyte or the catalyst, thereby compromising the measurements.

Capacitive background currents, which result from ion adsorption and desorption on the working electrode surface (electrical double layer currents) during CV measurements, should be removed to yield true kinetic currents for the ORR/OER. Such background currents in ORR measurements

Energy & Environmental Science Accepted Manuscript

 This journal is © The Royal Society of Chemistry 2012

can be removed by subtraction of current taken in an Ar- or N_2-saturated electrolyte from that in an O_2-saturated electrolyte (**Fig. 9c**). For the analysis of OER data, the background capacitive currents can be removed by averaging the forward ($dE/dt > 0$, $i_{DL} > 0$) and backward ($dE/dt < 0$, $i_{DL} < 0$) scan (**Fig. 9b**, light blue line), which assumes that the background capacitive currents are symmetric for the positive-going and negative-going sweeps.

Estimation of mass and specific activities

The kinetic current for the ORR/OER can be normalized by mass, electrocatalytic surface area, or the number of active sites of oxide catalysts to yield mass activity (applicable to oxide powder catalysts), specific activity, and TOF, respectively. Methods for the determination of the electrocatalytic surface area of oxide particles can be found in the work by Trassati and Petrii.[122] Common *ex situ* analyses of powder surface area are based on analysis of gas adsorption isotherms using Brunauer-Emmett-Teller (BET) theory[123], and particle sizes obtained from scanning electron or transition electron microscopy (SEM, TEM).[84, 116] *In situ* quantification of the surface area can also be obtained by measuring the double-layer capacitance (**Fig. 9c**) in a suitably small voltage range, which can be compared to the double-layer capacitance of a flat surface of the same material in identical electrolyte and experimental conditions. While the double-layer area-specific capacitance of oxides in basic solutions can vary from 22-130 μF/cm^2,[5, 124-136] 60 μF/cm^2 is a common estimate for oxide surfaces.[66, 137]

Tafel plots provide a convenient way of benchmarking materials for ORR and OER activities (**Fig. 9d**). In these plots, the overpotential is plotted versus the logarithm of the current density. The Tafel slope can give insight into the reaction mechanism[51, 95] and the intercept is known as the exchange current density (i.e. current at zero overpotential). However, for multiple electron reactions such as the ORR/OER, the exchange current cannot be determined reliably by Tafel analysis: in these cases, extrapolation from high overpotential regions to the reversible potential does not account for the potential dependence of the rate-limiting step(s).[138] Instead, it is most common to compare materials by their overpotential at a given current density (or conversely, current density at given overpotential). Ideally, only materials with identical Tafel slopes are compared so that the current density (or overpotential) can be chosen arbitrarily.

Relating the electronic structure of perovskite oxides to oxygen electrocatalysis

In this section, we discuss how identifying relationships between the ORR/OER activity and catalyst electronic structure can be used to gain new design strategies and mechanistic insights for oxide catalysts. We specifically focus on the use of one of the largest families of oxides – the perovskites – to establish guiding principles for oxygen electrocatalyst design based on electronic structure and explore the ORR/OER reaction mechanisms. Nearly all of the transition metals in the periodic table can be stabilized in the structure, making it ideally suited for exploring the influence of catalyst chemistry and electronic structure on the ORR/OER. The formula unit for the perovskite structure is ABO_3, where A and B are metal cations that occupy the cube corners and center, respectively, while oxygen anions occupy the cube faces. The B-site cations have six-fold oxygen coordination and are typically transition metal ions. The A-site cations have twelve-fold coordination and can accommodate alkaline, alkaline earth, and rare earth metal ions with valences from 1+ to 3+. The selection of A-site ions thus imposes constraints on B-site valence and oxygen non-stoichiometry by charge neutrality. Experimentally, the oxidation state of the transition metal ions in perovskites can be determined by X-ray absorption near-edge spectroscopy (XANES),[139, 140] X-ray photoelectron spectroscopy (XPS),[141, 142] electron energy loss spectroscopy (EELS),[143] and Mössbauer spectroscopy[144] in addition to thermogravimetric analysis[145, 146] and titration methods that employ redox-coupled back-titrant indicators.[147, 148]

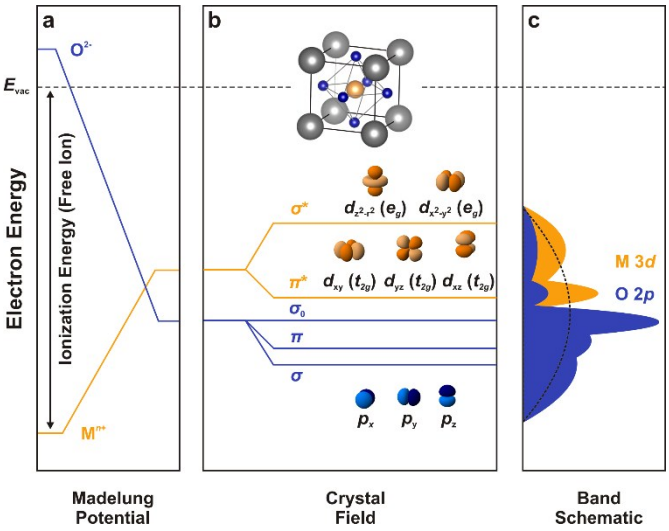

Fig. 10 Contributions to an oxide band structure for the perovskite structure (unit cell inset). Physical origins of shifts in constituent ion orbitals for oxides with octahedral oxygen coordination around transition metal ions. The dashed line represents the energy of free vacuum. (a) The energy of free ions in vacuum is determined by their ionization energy/electron affinity; the on-site Madelung potential of ions shifts these energies in the crystal lattice. (b) Asymmetric covalent mixing between M 3*d* and O 2*p* orbitals form σ- and π-bonding and anti-bonding orbitals (known as the "crystal field" interaction). Illustration of the M 3*d* and O 2*p* atomic orbitals. For octahedral coordination around the transition metal, the M 3*d* orbitals are split into e_g and t_{2g} states. (c) Schematic diagram of the one-electron band structure showing states with partial transition metal character (orange) and oxygen character (blue). Often, the three oxygen bands are shown as a single broad band indicated by the dashed curve.

Electronic structure factors of perovskites relevant to catalysis

Generally, one of the strongest influences on the electronic levels of metal oxides is the crystal structure, which results in an electrostatic potential for each unique crystallographic site

Energy & Environmental Science Accepted Manuscript

('Madelung Potential,' **Fig. 10**). Cations are surrounded by negatively charged oxygen anions, which generates a repulsive effect for electrons on the cations, raising their orbital energies. Conversely, oxygen anions are surrounded by positively charged cations, which generates an attractive effect for electrons, reducing the electron energy of oxygen anions. Thus, despite the fact that the electronegativities of free cations are higher than those of free anions, the Madelung potential can inverse the relative electron affinities of the ions in the crystal lattice and promote electron localization on the already negatively charged oxygen anions.[149] Through systematic studies within the perovskite family, this effect becomes secondary to the influence of transition metal (B-site) electronegativity, covalent bond character, and electron exchange interactions.[92, 150]

Although metal oxides were treated classically in the ionic limit,[92, 151] the metal-oxygen bonds in oxides have mixed ionic-covalent character,[152] which greatly influences the electronic structure. The most relevant electronic states for bond formation in oxides are the metal valence states (*d* electrons) and oxygen valence states (*p* electrons). Covalent mixing (hybridization) of the metal (M) *d* orbitals and O 2*p* orbitals occur due to the spatial overlap and energetic similarity of the electronic states. Due the octahedral environment, the $d_{z2\text{-}r2}$ and $d_{x2\text{-}y2}$ lobes of the transition metal *d* orbitals have strong spatial overlap with those of adjacent O 2*p* orbitals, forming σ-bonding and σ*-antibonding states with partial metal and oxygen character (referred to as e_g states). The d_{xy}, d_{yz}, and d_{xz} lobes have weaker spatial overlap with nearby O 2*p* orbitals and form π-bonds and π*-antibonds (referred to as t_{2g} states). The splitting of the *d* states into e_g and t_{2g} states is known as the crystal-field ('Crystal Field,' **Fig. 10**).[153] Some O 2*p* states do not hybridize with metal *d* states and thus form nominally non-bonding (σ_0) states, although these states still self-hybridize (i.e. 2*sp* hybridization) and bond with the *sp*-orbitals of other nearby O^{2-} ions. However, these non-bonding states alone do not contribute to the diversity of physical properties in oxides.

The molecular orbitals described above become bands in oxide crystals due to the translational symmetry of the unit cell, resulting in a M *d* band and O 2*p* band ('Band Schematic,' **Fig. 10**).[154, 155] However, it is important to note that the designation of "metal" and "oxygen" bands is used to describe the dominant character of the band; in reality, the metal *d*-bands in oxides are of mixed metal and oxygen parentage due to the hybridization of metal and oxygen states.

The degree of metal-oxygen hybridization is tuned by the choice of transition metal ion and its oxidation state, both of which modify the number of *d* electrons and the electronegativity of the metal ion. Moving across a row on the periodic table increases the number of *d* electrons and increases its electronegativity. Increasing the oxidation state decreases the number of *d* electrons and increases the metal ion electronegativity (due to reduced electron shielding). The electronegativity scales with the ionization energy of the transition metal ('Ionization Energy,' **Fig. 10**), which determines the energy of the transition metal *d* states. The degree of metal-oxygen hybridization in an oxide can be obtained using soft XANES.[152] Various works have proposed methods for quantifying the metal-oxygen covalent mixing from the O *K*-edge spectrum,[152, 156] which can be used to show that the transition metal electronegativity directly scales with the hybridization in perovskite oxides.[157] Increasing the transition metal electronegativity typically moves the metal *d* states closer in energy to the O 2*p* states, increasing the metal-oxygen hybridization and the ligand-field splitting, which plays a major role in the electronic properties of these oxides. For early transition metal perovskites (e.g. $LaCrO_3$), the metal ions are typically less electronegative than the oxygen ions.[92, 158] Thus, the M *d* band is higher in energy than the O 2*p* band, resulting in *antibonding* M *d* bands and *bonding* O 2*p* bands.

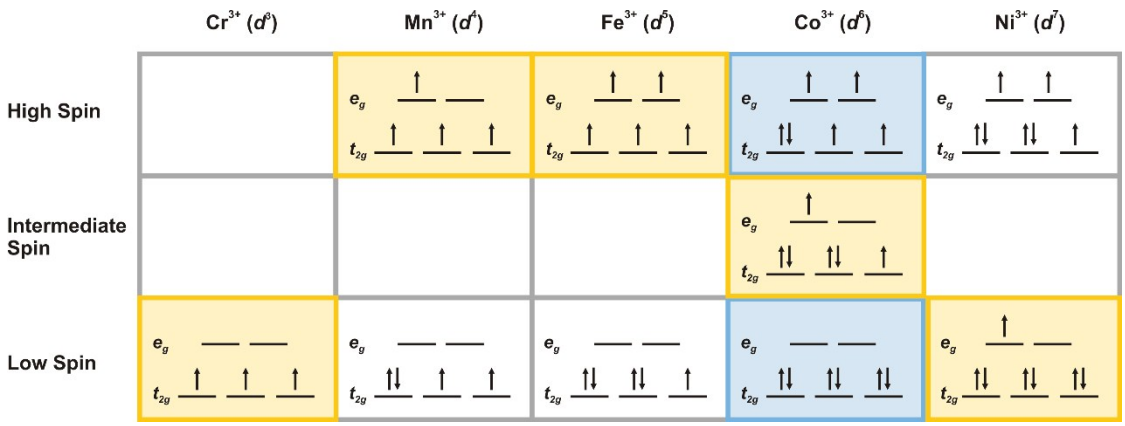

Fig. 11 Potential transition metal 3*d* (e_g and t_{2g} in Fig. 10) electron configurations for LaMO_3 perovskite oxides (*M* = Cr, Mn,[175] Fe,[176] Co,[177] Ni[178, 179]) for different spin states at room temperature. Orange configurations designate the stable spin state for the bulk oxide at room temperature as determined by magnetic measurements. White configurations are possible spin states observed at other temperatures or under thin film epitaxial strain. Although an intermediate spin state is typically cited as the stable electronic configuration for $LaCoO_3$ at room temperature, this remains controversial and thus the high and low spin configurations are shown in blue to emphasize the ambiguity of the cobalt spin state.[165, 180-183]

Energy & Environmental Science Accepted Manuscript

 This journal is © The Royal Society of Chemistry 2012

These oxides are typically insulating because the highest energy electrons are predominantly M *d* electrons, which are more localized than the O 2*p* electrons. Increasing the transition metal electronegativity can lower the M *d* states below that of the O 2*p* states[92, 159, 160], resulting in *bonding* M *d* bands and *antibonding* O 2*p* bands. Consequently, these oxides are semiconducting/metallic due to the large *p*-orbital character of electrons the highest energy electrons.

The electronic structure of oxides is also influenced by the relative occupancy of the e_g and t_{2g} states (referred to as the spin state). Because electrons of opposite spin occupying the same orbital experience Coulombic repulsion, there is a competition between electron pairing and filling the higher energy t_{2g} states. For *d* orbitals with splitting larger than the electron pairing energy, electrons completely occupy the lower energy t_{2g} states before filling the higher energy e_g states – known as a low-spin configuration. Conversely, when the splitting is smaller than the pairing energy, electrons occupy the e_g states prior to pairing in the t_{2g} states – known as a high-spin configuration.[153] Spin state has been shown to influence electronic conductivity[161], thermal expansion[162], bulk modulus[163], and catalytic activity.[164] The spin state of transition metal ions can be estimated, e.g., from the temperature-dependence of the magnetic susceptibility using molecular magnetism models[153] or X-ray absorption spectroscopy via the branching ratio of excited state multiplets.[165, 166]

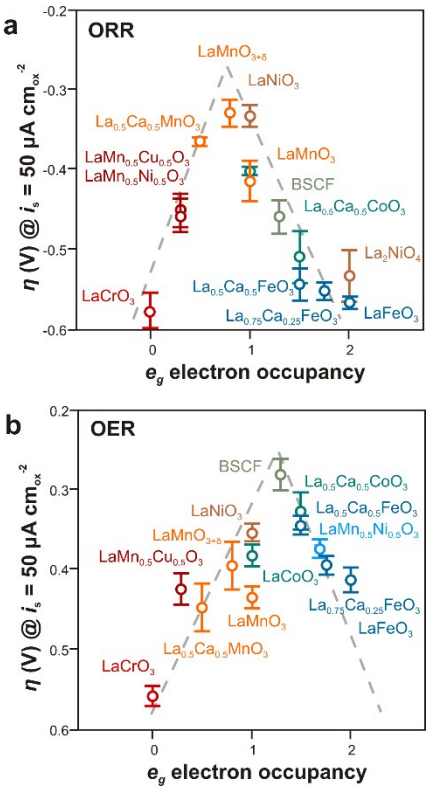

Fig. 12 The ORR and OER on various perovskite oxides in alkaline solution. (a) Overpotentials for the ORR as a function of e_g electron occupancy on various perovskites. (b) Overpotentials for the OER as a function of e_g electron occupancy on various perovskites. Figure adapted from refs. 164 and 67 with permission from Nature Publishing Group and AAAS.

ORR/OER activity descriptors for perovskites from molecular orbital principles

Molecular orbitals describing the electronic states of MO_6 octahedra in perovskites have seen success at explaining physical phenomena in oxides,[150, 167] especially on surfaces.[154, 168] Bockris and Otagawa (1984)[59, 87] first discussed one of the simplest electronic descriptors in their analysis of ABO_3 (B = Cr, V, Mn, Fe, Co, Ni) perovskite electrocatalysts – the number of transition metal *d* electrons.[66, 95] They found that the OER overpotential trended inversely with the enthalpy of hydroxide formation and *d*-electron number. Thus, they concluded that the number of *d* electrons is the primary influence on the OH* bond strength via the occupancy of the metal-OH antibonding levels. Conceptually, this is analogous to the *d*-band center model, which describes chemisorption strength by the relative occupancy of antibonding states. Interestingly, recent DFT-computed binding strengths of possible OER intermediates were later found to scale with the number of *d* electrons and oxidation state,[169] similar to the findings of Bockris and Otagawa.

Yet Bockris' and Otagawa's ideas stood in contrast to other works of the period linking chemical reaction rates on oxide surfaces to coordination chemistry concepts. Dowden (1972)[170] and Inai and Iwakura (1979)[171] both argued that the crystal field stabilization energy (CFSE) – the change in energy associated with the metal-ligand environment[172] – could be used to determine the activation energy of a catalyzed reaction. Dowden[170] postulated an M-shaped trend in chemisorption strength as a function of *d* electron number due to the dependence of the CFSE on the e_g occupancy. Such a trend was known at the time to influence the heats of hydration of transition metal cations in solution.[173] Specifically, Dowden predicted that in addition to the electronegativity trend, chemisorption would be enhanced by the CFSE at d^3 and d^8, and be minimally influenced at d^0, d^5, and d^{10}. Inai and Iwakura[171] suggested similar trends for chlorine evolution on oxide surfaces based on the change in CFSE associated with activated surface complexes. Dependence on the CFSE first emphasized the important dependence of the chemistry on the transition metal spin state. Subsequent studies by Larsson and Johansson (1990)[174] proposed an influence of the spin state on the ORR activity, observing correlations between the activity and magnetic moment.

The oxidation state and spin state of the B-site in the perovskite structure are therefore both important considerations for understanding trends in chemisorption strength on perovskite surfaces. Typical spin states for La*M*O_3 (*M* = Cr, Mn,[175] Fe,[176] Co,[177] Ni[178, 179]) at room temperature are well known, and the *d*-electron configurations of these oxides are shown in **Fig. 11**. It was only recently that principles from coordination chemistry were revisited once more to rationalize differences in catalytic activity among oxides with

Energy & Environmental Science Accepted Manuscript

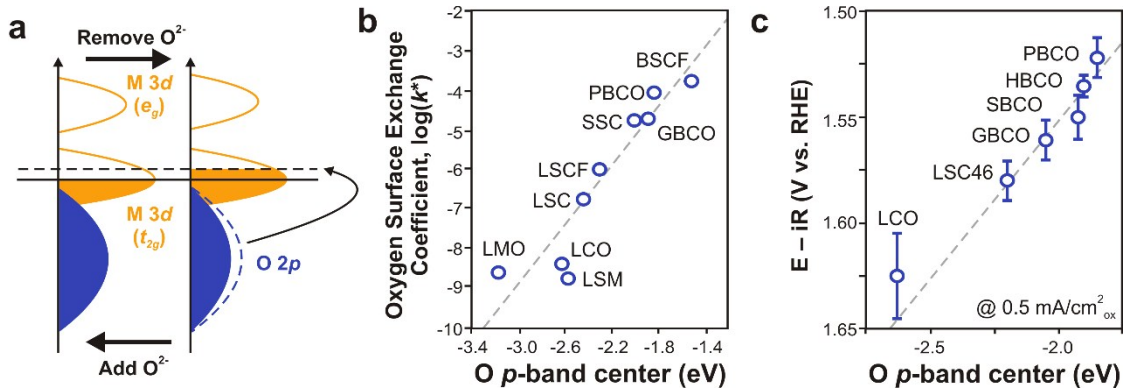

Fig. 13 Theory and role of the O *p*-band center in describing oxygen surface exchange on perovskite catalysts. (a) Schematic illustration of perovskite density of states, showing the transition metal 3*d* (orange) and O 2*p* (blue) bands. In the rigid band model, when oxygen is removed from the lattice, the O 2*p* states decrease in density and the consequent increase in bulk electron density results in an upshift of the Fermi level (horizontal solid and dashed lines). The opposite holds true when an oxygen vacancy is filled. (b) Linear relationship between the measured oxygen surface exchange coefficient (T = 1000 K, $p(O_2)$ = 0.2 – 1.0 bar) and calculated O *p*-band center for perovskites. Figure adapted from ref. 202 with permission by the Royal Chemical Society. (c) Trend of the OER activity (potential at 0.5 mA/cm $_{ox}$ ^{2}) with the calculated O *p*-band center relative to the Fermi level for $LaCoO_3$ (LCO), $La_{0.4}Sr_{0.6}CoO_{3-\delta}$ (LSC46), $GdBaCo_2O_{5+\delta}$ (GBCO), $SmBaCo_2O_{5+\delta}$ (SBCO), $HoBaCo_2O_{5+\delta}$ (HBCO), and $PrBaCo_2O_{5+\delta}$ (PBCO). Figure adapted from ref. 36 with permission from Nature Publishing group.

considerations of both the transition metal electronegativity and the spin state. Through the application of thin film RDE, our work demonstrated that both the ORR and OER activity of perovskite oxides[67, 164] follows a volcano relationship with the occupancy of the e_g electronic states (**Fig. 12a** and **12b**). As a secondary descriptor for oxides with similar e_g occupancy, the activity trended with the transition metal electronegativity (e.g. Ni > Co > Mn).[157]

The e_g-occupancy activity descriptor postulates that the number of electrons in the σ^* states determines the metal-oxygen bond strength, reducing the thermodynamic overpotential of ORR/OER on oxide surfaces along the lines of the Sabatier principle. Oxides that have too low an e_g occupancy (e_g < 1) bind to oxygen too strongly, while oxides that have too high an e_g occupancy (e_g > 1) bind too weakly. The e_g occupancy model was the first demonstration of chemisorption trends from classical coordination chemistry. In contrast to the *d*-electron OER descriptor from Bockris and Otagawa, the e_g occupancy assumes that the σ-interaction of the e_g states dominates over the weaker π-interaction of the t_{2g} states. Additionally, the occupancy is not the sole determining factor – electronegativity (the energy level of the transition metal 3*d* states) also serves as a secondary descriptor.

These studies also revealed an asymmetry in the ORR/OER trends among perovskite catalysts. While e_g occupancy slightly less than 1 is favorable for the ORR, an occupancy slightly greater than 1 is preferable for the OER (**Fig. 12**). This highlights one of the central challenges in developing bifunctional catalysts for devices capable of both converting and storing energy.

New experiments remain to be developed for accurately measuring the e_g occupancy of oxides, especially for the surface during the ORR/OER. The estimation of the e_g occupancy in our previous studies[67, 164] was based on the oxidation state and spin state extracted from bulk-sensitive measurements – namely hard X-ray absorption and magnetometry. Several studies have shown that conventional oxidation state and spin state measurements may not reflect the underlying atomic states; for example, the bulk atomic states of cobalt-based perovskites remain the subject of great debate.[165, 180-183]

ORR/OER activity descriptors for perovskites from band theory

While qualitatively useful, molecular orbital approximations are only accurate when the metal-oxygen bonds are nearly ionic,[90] which suggests that more involved treatments may be necessary to identify more robust activity descriptors. As the *d*-band center model demonstrated, bulk band descriptions of the electronic states can provide useful insights into surface adsorbate interactions.

Band descriptions of the oxide electronic structure were first employed as a descriptor by Meadowcroft in 1970.[184] In his seminal investigation of perovskites for the ORR, Meadowcroft speculated that oxides that can be both *n*-type or *p*-type – such as $LaCoO_3$ – behave amphoterically, capable of reacting as either a Lewis acid or base and supporting both chemisorption and release of adsorbates. More refined understanding of oxide electronic structure beyond classical semiconductor models were developed in the late 1960s and through the 1970s,[154, 167, 168, 185-188] leading to their first application as ORR/OER catalyst descriptors by Matsumoto and co-workers (1977-1986).[189-197] They first postulated that the delocalization of the σ^* (e_g) states into bands and its filling determines electron transfer rates for the ORR.[190] Using electronic configurations of the metal *d* states proposed by Goodenough and co-workers,[198] they provided a qualitative ranking of perovskite ORR catalysts.[189-192] Wattiaux et al. (1987)[199, 200] examined these concepts in more detail through a systematic study of $La_{1-x}Sr_xFeO_{3-\delta}$ and verified that the OER activity also scaled with the concentration of delocalized electrons. The number of σ^* electrons and the

Energy & Environmental Science Accepted Manuscript

 This journal is © The Royal Society of Chemistry 2012

metal-oxygen hybridization are the solid-state analogues to the e_g occupancy descriptor discussed above.

Matsumoto et al. later revisited to these concepts and specifically proposed that the width of the σ^* bands plays a central role in oxygen electrocatalysis, as the band width reflects the electron mobility of the oxide.[193-197] The role of band width in surface redox reactions was further investigated spectroscopically by Egdell et al. (1983).[201] However, they came to the opposite conclusion: although broadening of the bands improves electron transport within the solid, they found that narrow bands are needed to reduce the overpotential of Ru^{IV}/Ru^{V} redox couples in perovskite and pyrochlore ruthenates.[201] The reduction of the Ru band width helps to stabilize localized charge at the surface active sites, thus facilitating electron transfer at the electrode-electrolyte interface. These findings thus highlight a need for more exact treatments of the band structure and surface reactions.

Developments in DFT have opened new doors in linking electrocatalytic activity with electronic structure. Our recent work demonstrated that the position of the bulk O *p*-band center relative to the Fermi level correlates strongly with the oxygen surface exchange kinetics (**Fig. 13a and 13b**).[202] In a similar fashion, the computed O *p*-band center also correlates with experimental OER activities of cobalt-based perovskites in alkaline solution, as shown in **Fig. 13c**.[36] The O *p*-band center descriptor for OER can be related to tuning the intermediate energies of Mechanisms **7a** or **7b** in **Fig. 7** (one-metal-site mechanisms), as previous work verified that the O *p*-band center scales with oxygen adsorption strength on the surface.[202] As a design parameter, the O *p*-band center descriptor reflects differences in the Fermi energy of the oxide, as the absolute energy of the O *p*-band largely depends on the Madelung potential and oxygen electron affinity (neither of which changes significantly within the perovskite family). The Fermi level can be pushed closer to the O *p*-band center by increasing the electronegativity of the transition metal (which lowers the metal *d* band); this can be done by increasing the oxidation state or substitution of the transition metal.[203] Further spectroscopic experiments are needed to investigate the metal and oxygen states to verify the computed trends and design rationale.

Stability of oxide surfaces during oxygen electrocatalysis

Stable catalyst surfaces are of paramount importance in preserving catalytic activity as well as accurate understanding of the relationship between activity and descriptors of catalysts. In Pt-based catalysts, the stability of alloyed surfaces in acid has been a major obstacle in enhancing catalytic activity.[8, 75, 204] Despite their bulk stability in alkaline electrolytes, oxide surfaces are susceptible to extensive hydroxylation,[205, 206] reconstruction,[207-209] and decomposition.[210, 211] Short-term testing of long-term catalyst stability has been a particular challenge. However, Frydendal et al.[212] recently demonstrated that while short-term chronopotentiometry and chronoamperometry measurements are not indicative of long-term performance stability, electrochemical quartz crystal microbalance (EQCM) and inductively coupled mass spectroscopy (ICP-MS) offer a meaningful alternative to long-term device testing. ICP-MS studies have confirmed that degradation of RuO_2,[212] MnO_x,[212] and $SrRuO_3$[213] are due to anodic dissolution, forming transition metal species in solution. It is essential that new methods be further developed for characterizing dissolution mechanisms and identifying the relationships between catalyst stability and chemistry.

Although the surfaces of oxides are challenging to understand, bulk stability can be more easily rationalized. Powders of $LaMnO_3$ (LMO), $LaCoO_3$ (LCO), and $La_{0.4}Sr_{0.6}CoO_{3-\delta}$ (LSC46) are all structurally stable after cycling at OER potentials. However, $Ba_{0.5}Sr_{0.5}Co_{0.8}Fe_{0.2}O_{3-\delta}$ (BSCF82) powders undergo quick amorphization that ultimately penetrate deep into the material (**Fig. 14**), accompanied by decreased surface concentrations of Ba^{2+} and Sr^{2+} ions and increased pseudocapacitance and OER currents.[210] Similar effects were also observed in $Ba_{0.5}Sr_{0.5}Co_{0.4}Fe_{0.6}O_{3-\delta}$ (BSCF46) and $SrCo_{0.8}Fe_{0.2}O_{3-\delta}$ (SCF82).

A common method for rationalizing the relative stability of perovskites is to consider the Goldschmidt tolerance factor,[214] which is defined as:

$$\tau = \frac{r_A + r_O}{\sqrt{2}(r_B + r_O)}$$

(where r_A, r_B, and r_O are the ionic radii for the A-site, B-site, and O^{2-} ions respectively). The ideal cubic structure is most stable when $\tau = 1$, i.e. the A-site cation is similar in size to the O^{2-} ions to form close-packed layers and the B-site cation matches the octahedral interstitial size. For $\tau < 1$, pseudocubic structures with tilted BO_6 octahedra are generally stabilized, while for $\tau > 1$, hexagonal structures may form.[215] It is also possible for perovskites with $\tau > 1$ to form in the cubic phase if oxygen vacancies can be introduced. Assuming that the oxides become fully oxidized under the highly oxidizing conditions of the OER at pH 13 (i.e. with $\delta = 0$), the large ionic radii of Ba^{2+} and Sr^{2+}, coupled with the small Co^{4+} and Fe^{4+} radii, strongly destabilize this class of perovskites due to their large tolerance factors (**Fig. 14b**, orange). Conversely, the La-based perovskites are stabilized due to the smaller La cationic radius and lower transition metal oxidation states.[216] This is further supported by the improved stability of BSCF with the substitution of Ba and Sr with La ions.[216]

Interestingly, the amorphization of these perovskites also correlates well with the O *p*-band center (again with the fully oxidized chemistry; **Fig. 14b**, blue), which may act as a useful descriptor of oxide stability due to its relationship with the bulk oxygen vacancy formation energy – namely, as the O *p*-band center moves closer to the Fermi level, the oxygen vacancy formation energy decreases, potentially destabilizing the perovskite phase.[36, 210, 217]

Energy & Environmental Science Accepted Manuscript

These studies highlight the importance of considering surface stability of oxides under oxygen electrochemical reaction conditions, as well as some basic methods for rationalizing the relative stabilities of different chemistries.

Perspectives and outlook

Although numerous activity descriptors have been proposed from the study of oxide ceramics, composite oxide/carbon/Nafion® electrodes, and first-principles calculations, many fundamental scientific questions regarding the ORR/OER mechanism(s) on oxide surfaces remain unanswered. It should be noted that the relative catalytic performance of different oxides for Li_2O_2 oxidation is known to differ drastically from H_2O oxidation in alkaline solution,[218] which suggests that chemical design principles for the OER may differ in metal-air systems. Similarly, oxide catalysts for heterogeneous ORR catalysis in solid-state devices have different trends in ORR performance from in alkaline solution.[164, 202] Thus, the broad application of the design principles discussed thus far in this Review must be cautioned, as the mechanisms underlying these reactions may be quite different.[9] Such differences among these apparently similar yet empirically disparate fields emphasize a need for more detailed understanding of the differentiating factors in alkaline electrocatalysis. In particular, the nature of the active site and its interaction with oxygen and water, the role of proton-coupled electron transfers (PCETs) during the ORR/OER, and the orientation-dependence of catalytic activity are all poorly defined in such heterogeneous systems. The study of well-defined surfaces of model systems and the use of in situ spectroscopic techniques can bring new understanding to these areas, guiding future design of commercially relevant high surface area nanoparticles.

Well-defined transition metal oxide surfaces

Leveraging recent advances in fabricating heterojunctions and well-defined oxide surfaces can provide insights into active sites on the atomic level. Single-crystal surfaces can be produced by growing epitaxial thin films of oxides on single crystal substrates using pulsed laser deposition (PLD) or molecular beam epitaxy (MBE). Studies of such thin films and herostructures have revolutionized our understanding of oxide physics in the past decade.[219, 220]

Despite the great prospects of utilizing oriented thin films as model oxide surfaces (akin to the fundamental study of metallic single crystals), electrocatalytic studies of well-defined surfaces are still rare compared to studies of powders or textured films. In general, activity differences between films and powders could be caused by differences in the oxygen stoichiometry, uncertainty in the crystallographic planes exposed on the oxide surface, and/or additives in the ink used to cast oxide powders. Despite these complications, we have shown in several publications[37, 120] that the ORR and OER activities of epitaxial oxide thin films can be comparable to those of ink-casted oxide powders (**Fig. 15**). Discrepancies in the OER currents observed in LMO and LSMO may arise due to the electronic transport across the catalyst/substrate interface[221] or possibly dissolution currents. This is in contrast to a study by Miyahara et al.,[222] which found that 200 nm thick oxide films have comparable OER, but lower ORR activity compared to composite

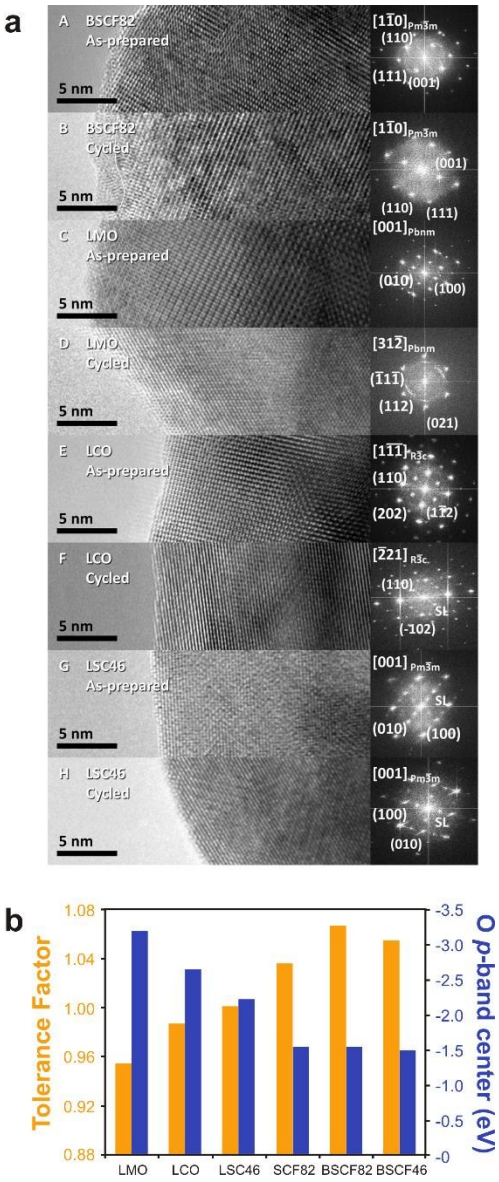

Fig. 14 Stability of various perovskite oxides under anodic potential cycling for the OER in alkaline solution. (a) High-resolution transmission electron microscopy (HRTEM) and fast Fourier transforms (FFT) of (A) as-prepared $Ba_{0.5}Sr_{0.5}Co_{0.8}Fe_{0.2}O_{3-\delta}$ (BSCF82) powder and (B) cycled electrode, (C) as-prepared $LaMnO_3$ (LMO) powder and (D) cycled electrode, (E) as-prepared $LaCoO_3$ (LCO) powder and (F) cycled electrode, and (G) as-prepared $La_{0.4}Sr_{0.6}CoO_{3-\delta}$ (LSC46) powder and (H) cycled electrode. BSCF82 forms an amorphous region near the surface quickly after cycling as indicated by the dotted line. (b) Tolerance factors and O *p*-band center positions for the various perovskites. A correlation is observed that perovskites with tolerance factor larger than 1 (typically observed in the hexagonal perovskite phase) and O *p*-band center above −2.2 eV become amorphous at the surface upon cycling. Figure adapted from ref. 210 with permission from the American Chemical Society.

Energy & Environmental Science Accepted Manuscript

This journal is © The Royal Society of Chemistry 2012

electrodes. Although the resistivity in their films did not affect the diffusion-limited current in RDE measurements, it was much greater than that of the films shown in **Fig. 15**. Catalyst-support interactions have also been also been found to play a notable role in the study of $(001)_{pc}$-oriented $LaMnO_{3\pm\delta}$ ("pc" denotes the pseudocubic unit cell), where decreasing the film thickness from 10 to 1 nm led to a dramatic reduction in activity, attributed in part to charge-transfer from the Nb:$SrTiO_3$ substrate.[120] Such measurements highlight the importance of the support, whether for reducing electronic transport limitations or catalyzing the reaction.

The use of well-defined interfaces and surfaces can identify bifunctional catalysts for the ORR and OER. Recently, heterostructured BSCF82-on-$La_{0.8}Sr_{0.2}MnO_{3-\delta}$ (LSMO) thin films provided a clearly defined two-component surface with a combined overpotential that rivals the state-of-the-art bifunctional catalysts in literature,[37] and enhanced ORR stability relative to bare LSMO films. Moreover, the co-deposition of oxide thin films can result in marked enhancement in the surface oxygen exchange kinetics[223-225] as well as stability.[225-227] Therefore, heterostructured surfaces can provide new opportunities for developing oxide electrocatalysts with improved activity and stability and identifying the active components in multi-material systems.

Single-crystal surfaces are also ideally suited to study the effect of crystallographic orientation on catalytic activity. Our recent OER studies on rutile RuO_2 and IrO_2 thin films has found that the (100) surfaces are more active for OER than the (110) surfaces in alkaline solution. The OER current is correlated with the higher utilization of active sites on the more open (100) orientation.[34] Komo et al.[228] performed similar studies on the ORR/OER activities among the $(001)_{pc}$, $(110)_{pc}$, and $(111)_{pc}$ surfaces of 30 nm $La_{0.8}Sr_{0.2}CoO_{3-\delta}$ thin films grown on $SrTiO_3$, finding the $(110)_{pc}$ surface as the most active for both the ORR and OER. This trend in activity paralleled the degree of oxygen vacancy formation, where the $(110)_{pc}$ film had the largest lattice expansion measured post-cycling.

Well-defined surfaces open new doors to exploring the activity of different surfaces, but also their stability during oxygen electrocatalysis. Chang et al.[213] probed the relationship between orientation and activity for $SrRuO_3$ thin films, finding a dramatic destabilization of the most active $(111)_{pc}$ surface. The low surface energy, non-polar $(001)_{pc}$ surface was the most stable but least active, while the more defective and undercoordinated $(111)_{pc}$ and $(110)_{pc}$ surfaces were more active but exhibited increased cation dissolution. In contrast to BSCF powders and films, these $SrRuO_3$ films exhibited complete loss of the active site within the first cycle at higher overpotentials, while BSCF retains active sites (although they may differ in number and chemistry over time). Additional studies are needed to better understand the surface oxide atomic and electronic structure changes during the ORR and OER in order to develop more general principles for how they influence oxide activity and stability.

We caution that thin film surfaces can open new phenomena induced by epitaxial strain, vacancy defects, and/or the deposition method that may influence the catalytic activity. For instance, growth of $LaCoO_3$ thin films on different substrates has been used to identify a strain-induced ferromagnetic ground state that is not present in bulk.[229, 230] This influence of strain on the magnetic properties of the film directly modifies the cobalt ion spin state, which changes the oxygen vacancy formation energetics and catalytic properties towards oxygen reduction and evolution.[231] Strong cation segregation in perovskite thin films can also play an important role in modifying the surface chemistry relative to bulk systems.[231-233] Future studies are needed to consider these factors in studying oxygen electrocatalysis on surfaces of oxide thin films.

In situ spectroscopic approaches

In situ spectroscopic studies including X-ray absorption near-edge spectroscopy (XANES),[234-236] extended X-ray absorption fine structure spectroscopy (EXAFS),[237-239] Fourier transform

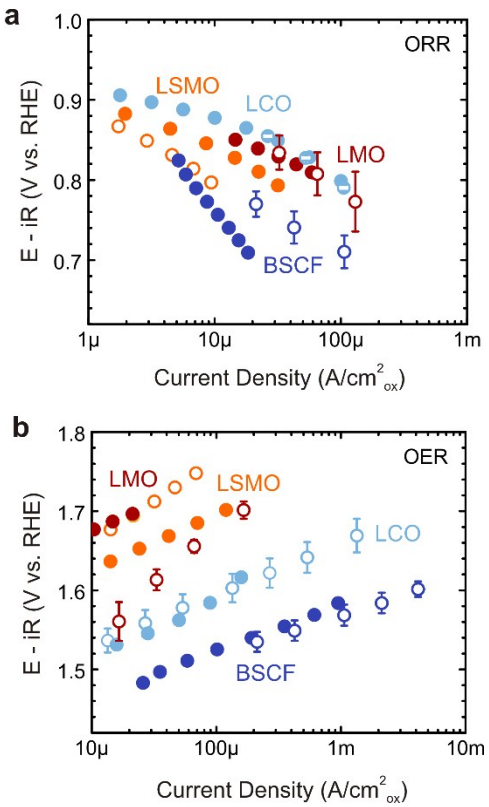

Fig. 15 Comparison between the activities of $(001)_{pseudocubic}$-oriented thin films (solid symbols) and powders (open symbols) with nominally identical chemistry in O_2-saturated 0.1 M KOH. (a) Tafel plot of the ORR activity of $LaMnO_{3\pm\delta}$ (LMO; red; data from refs. 120 and 164), $La_{0.8}Sr_{0.2}MnO_{3-\delta}$ (LSMO; orange; data from refs. 120 and 164), $LaCoO_3$ (LCO; light blue; powder data from ref. 164) and $Ba_{0.5}Sr_{0.5}Co_{0.8}Fe_{0.2}O_{3-\delta}$ (BSCF; dark blue; data from refs. 37) on LSMO. (b) Tafel plot of the OER activity of LSMO and BSCF (data from refs. 37 and 67. All thin films were deposited on Nb-doped $SrTiO_3$ substrates by pulsed-laser deposition (PLD). Powders were ink-casted onto glassy carbon electrodes (oxide:carbon:Nafion = 1:5:5) and rotated at 1600 rpm. The oxide areas of BSCF and LSMO powders were determined by BET and the oxide area of LMO and LCO by SEM analysis. Error bars represent the standard deviation of at least 3 independently prepared electrodes.

Energy & Environmental Science Accepted Manuscript

infrared spectroscopy (FT-IR),[235, 236] and Raman spectroscopy[240] have been widely used to probe reaction mechanisms of catalytic processes of gas molecules such as CO oxidation. Bulk-sensitive techniques such as XANES and EXAFS[241, 242] have been used to explore oxide stability and transition metal oxidation state. These techniques are particularly insightful for exploring structural changes, such as amorphization under OER conditions.[210, 243]

Combining well-defined surfaces and recent advances in spectroscopy provides exciting new opportunities to probe dynamic changes of oxide surfaces relevant to the ORR/OER. Recent advances in ambient pressure X-ray photoemission spectroscopy (AP-XPS)[244-248] have enabled researchers to distinguish adsorbates on the surface and determine their coverage under conditions relevant to catalysis.[249-251] AP-XPS studies of surface wetting is also an important step toward understanding the reactivity of water molecules on oxide surfaces, and can provide new insights into how the surface electronic structure influences the coverage of intermediates. Although the technique has been extensively used in exploring water dissociation, adsorption, and wetting of well-defined metal films as a function of relative humidity,[252] studies of oxides have only recently begun, focusing largely on binary oxides that are inactive for the ORR/OER. For example, Yamamoto et al.[253] and Newberg et al.[254] have shown that dissociative adsorption and surface hydroxylation dominate water interactions on single crystal α-Fe_2O_3(0001) and MgO(100) thin film surfaces at low relative humidity while molecular water begins to adsorb at higher relative humidity, as shown in **Figure 16**. Understanding the degree of hydroxylation on catalytically active oxide surfaces such as perovskite surfaces could provide valuable mechanistic insights for the ORR/OER.

In situ X-ray reflectivity[227, 255] and scattering[74, 213, 255-257] offer new directions to study dynamic structural changes of well-defined oxide surfaces during the ORR/OER. X-ray reflectivity can be used to obtain information on the thickness and roughness of distinct chemical layers (e.g. CuO and Cu) on the order of tens of Angstroms.[255] For atomic-level structural information, in situ surface X-ray scattering (SXS) has been used extensively to probe the surfaces of noble metal electrodes, using model fitting to extract information on atomic layer-by-layer compositions of alloys,[74] reconstructed surface structures,[258] and adsorbate coverages and structures.[259, 260] These methods have been further applied to understanding simple oxide surfaces, such as the surface hydroxylation of hydrated α-Al_2O_3 (0001).[261] However, modeling the surfaces of ternary oxides is exceptionally difficult due to the various forms of surface reconstruction. To overcome this, three-dimensional reconstruction of oxide surface and sub-surface structures have been consistently demonstrated using Coherent Bragg Rod Analysis (COBRA)[262, 263] – a phase-retrieval method that combines information from multiple crystal truncation rods to determine the crystal structure near the surface. Such studies have been applied to understanding electrocatalysis in solid oxide fuel cell applications[232, 264] and

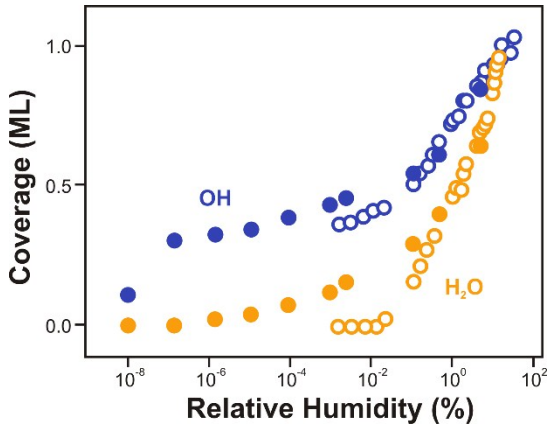

Figure 16. Coverages of OH and H_2O on α-Fe_2O_3(0001) as a function of relative humidity on a logarithmic scale. Relative humidity is defined as $p'/p_v(T) \times 100$, where p_v is the equilibrium vapor pressure of bulk water at the sample surface temperature. The coverages of OH (filled symbols) and H_2O (open symbols) were obtained from an isotherm, T = 295 K (blue), and an isobar, $p(H_2O)$ = 1 Torr (orange). Figure adapted from ref. 253 with permission from the American Chemical Society.

oxide electronics,[233, 265-267] and could greatly benefit the study of oxide surfaces for the ORR/OER in alkaline solutions. However, the low atomic number of oxygen results in weak scattering, making X-ray scattering techniques better suited for studying the catalyst surface structure rather than the adsorbate structure. In addition, weak scattering makes it difficult to identify the oxygen adsorbate speciation of the surface. Furthering understanding of the ORR/OER and catalyst surface chemistry therefore requires the synthesis of information from the various techniques discussed in this section.

Summary and conclusions

Improving the slow kinetics of oxygen electrocatalyis is a grand challenge that must be solved to make fuel cells, electrolyzers and metal-air batteries more commercially viable. The descriptor approach has proven fruitful to gain much needed insight into the electrocatalysis of oxygen, first on metals and later on oxides. In this Review, we have overviewed the evolution of descriptors for the ORR and OER on non-precious transition metal perovskite oxide electrocatalysts. The identification of electronic structure parameters associated with the adsorbate binding strength can provide simple rationale for the influence of composition on the electrocatalytic activity with the potential to predict new catalyst chemistries with enhanced activity. The core concepts we have discussed here can be extended to other oxide families, and possibly other transition-metal-based inorganic materials as well. As such, the stage is currently set for developing more detailed insights in the rational design of future electrocatalysts.

Two aspects of oxygen electrocatalysis on oxide surfaces distinguish the field from the study of metal catalysts, requiring

Energy & Environmental Science Accepted Manuscript

 This journal is © The Royal Society of Chemistry 2012

novel approaches for further investigation. First, the large body of proposed mechanisms for perovskite surfaces to date highlights the ambiguity of the reaction mechanism. Refining experiments to develop better understanding of the mechanism and how it differs with catalyst chemistry is a key step toward understanding oxygen electrocatalysis on oxide surfaces. Second, the stability of electrocatalysts remains an important issue for oxides, even in alkaline environments. We discuss how to extend the descriptor approach to the rational design of stable ORR/OER catalysts. Understanding these two central issues will require the use of improved model surfaces and new experimental techniques. The use of oxide thin films as well-defined surfaces can provide more accurate measurement of intrinsic catalytic activity and generate new insights on the electrocatalytic properties of different crystal facets. The development of new in situ spectroscopic techniques also creates new opportunities for detailed investigations, mechanistic insights, and probing of the relationship between electronic structure, adsorbate binding strength, and electrocatalytic activity.

The descriptor approach is only one of the many approaches for oxygen electrocatalyst design. New understanding comes from the outlook we have synthesized here, as well as from other methods, such as high-throughput computational and combinatorial screening. Exploration of new material chemistries will also inform more general design principles for rational catalyst design. Iterative improvements based on the findings from these different approaches are essential for developing strategies to realize the industrial application of efficient oxygen electrocatalysts for electrochemical energy storage and conversion technologies.

Acknowledgements

This work was supported in part by the MRSEC Program of the National Science Foundation under award number DMR-0819762 and the Skoltech-MIT Center for Electrochemical Energy. We acknowledge collaborations with Toyota North America Technical Center. K.A.S. was supported by the National Science Foundation Graduate Research Fellowship under Grant no. DGE-1122374.

Notes and References

1. J. O. Bockris and A. K. N. Reddy, *Modern Electrochemistry 1: Ionics*, Plenum Press, New York, 1998.
2. Y.-C. Lu, B. M. Gallant, D. G. Kwabi, J. R. Harding, R. R. Mitchell, M. S. Whittingham and Y. Shao-Horn, *Energy Environ. Sci*, 2013, **6**, 750.
3. G. Girishkumar, B. McCloskey, A. C. Luntz, S. Swanson and W. Wilcke, *J. Phys. Chem. Lett.*, 2010, **1**, 2193-2203.
4. J.-G. Zhang, P. G. Bruce and X. G. Zhang, in *Handbook fo Battery Materials, Second Edition*, eds. C. Daniel and J. O. Besenhard, Wiley-VCH Verlag GmBH & Co. KGaA, Weinheim, Germany, 2011.
5. C. C. McCrory, S. Jung, J. C. Peters and T. F. Jaramillo, *J. Am. Chem. Soc.*, 2013, **135**, 16977-16987.
6. M. G. Walter, E. L. Warren, J. R. McKone, S. W. Boettcher, Q. X. Mi, E. A. Santori and N. S. Lewis, *Chem. Rev.*, 2010, **110**, 6446-6473.
7. S. Y. Reece, J. A. Hamel, K. Sung, T. D. Jarvi, A. J. Esswein, J. J. H. Pijpers and D. G. Nocera, *Science*, 2011, **334**, 645-648.
8. H. A. Gasteiger, S. S. Kocha, B. Sompalli and F. T. Wagner, *Appl. Catal., B*, 2005, **56**, 9-35.
9. S. Adler, *Chem. Rev.*, 2004, **104**, 4791-4843.
10. N. S. Lewis and D. G. Nocera, *Proc. Natl. Acad. Sci. U. S. A.*, 2006, **103**, 15729-15735.
11. H. Dau, C. Limberg, T. Reier, M. Risch, S. Roggan and P. Strasser, *ChemCatChem*, 2010, **2**, 724-761.
12. T. R. Cook, D. K. Dogutan, S. Y. Reece, Y. Surendranath, T. S. Teets and D. G. Nocera, *Chem. Rev.*, 2010, **110**, 6474-6502.
13. M. Armand and J. M. Tarascon, *Nature*, 2008, **451**, 652-657.
14. Y. C. Lu, Z. C. Xu, H. A. Gasteiger, S. Chen, K. Hamad-Schifferli and Y. Shao-Horn, *J. Am. Chem. Soc.*, 2010, **132**, 12170-12171.
15. R. Cao, J.-S. Lee, M. Liu and J. Cho, *Adv. Energy Mater.*, 2012, **2**, 816-829.
16. H. A. Gasteiger and N. M. Markovic, *Science*, 2009, **324**, 48-49.
17. M. Piana, S. Catanorchi and H. A. Gasteiger, *Proton Exchange Membrane Fuel Cells 8, Pts 1 and 2*, Electrochemical Society Inc, Pennington, 2008.
18. A. Filpi, M. Boccia and H. A. Gasteiger, *ECS Trans.*, 2008, **16**, 1835-1845.
19. H. B. Beer, *J. Electrochem. Soc.*, 1980, **127**, 303C-307C.
20. P. G. Bruce, S. A. Freunberger, L. J. Hardwick and J. M. Tarascon, *Nat. Mater.*, 2012, **11**, 19-29.
21. G. M. Whitesides and G. W. Crabtree, *Science*, 2007, **315**, 796-798.
22. H. A. Gasteiger, D. R. Baker and R. N. Carter, *Hydrogen Fuel Cells: Fundamentals and Applications*, Wiley-CPH, 2010.
23. W. C. Chueh and S. M. Haile, *Annu. Rev. Chem. Biomol. Eng.*, 2012, **3**, 313-341.
24. P. Vanysek, in *CRC Handbook of Chemistry and Physics*, 92nd edn., 2000.
25. A. D. Mcnaught and A. Wilkinson, 2nd edn., 1997.
26. I. E. L. Stephens, A. S. Bondarenko, U. Gronbjerg, J. Rossmeisl and I. Chorkendorff, *Energy Environ. Sci*, 2012, **5**, 6744-6762.
27. B. Han, C. Carlton, A. Kongkanand, R. S. Kukreja, B. R. Theobald, L. Gan, R. O'Malley, P. Strasser, F. T. Wagner and Y. Shao-Horn, *Energy Environ. Sci*, 2014, **DOI: 10.1039/C4EE02144D**.
28. C. Chen, Y. Kang, Z. Huo, Z. Zhu, W. Huang, H. L. Xin, J. D. Snyder, D. Li, J. A. Herron, M. Mavrikakis, M. Chi, K. L. More, Y. Li, N. M. Markovic, G. A. Somorjai, P. Yang and V. R. Stamenkovic, *Science*, 2014, **343**, 1339-1343.
29. C. Cui, L. Gan, M. Heggen, S. Rudi and P. Strasser, *Nat. Mater.*, 2013, **12**, 766-771.
30. U. S. G. Survey, ed. U. S. G. Survey, 2014, p. 196.
31. Y. Lee, J. Suntivich, K. J. May, E. E. Perry and Y. Shao-Horn, *J. Phys. Chem. Lett.*, 2012, **3**, 399–404.
32. P. C. K. Vesborg and T. F. Jaramillo, *RSC Advances*, 2012, **2**, 7933.

Energy & Environmental Science Accepted Manuscript

33. I. Roche, E. Chainet, M. Chatenet and J. Vondrak, *J. Phys. Chem. C*, 2007, **111**, 1434-1443.
34. K. A. Stoerzinger, L. Qiao, M. D. Biegalski and Y. Shao-Horn, *J. Phys. Chem. Lett.*, 2014, 1636-1641.
35. A. Grimaud, C. E. Carlton, M. Risch, W. T. Hong, K. J. May and Y. Shao-Horn, *J. Phys. Chem. C*, 2013, **117**, 25926-25932.
36. A. Grimaud, K. J. May, C. E. Carlton, Y. L. Lee, M. Risch, W. T. Hong, J. Zhou and Y. Shao-Horn, *Nat. Commun.*, 2013, **4**, 2439.
37. M. Risch, K. A. Stoerzinger, S. Maruyama, W. T. Hong, I. Takeuchi and Y. Shao-Horn, *J. Am. Chem. Soc.*, 2014, **136**, 5229-5232.
38. M. W. Kanan and D. G. Nocera, *Science*, 2008, **321**, 1072-1075.
39. S. W. Lee, C. Carlton, M. Risch, Y. Surendranath, S. Chen, S. Furutsuki, A. Yamada, D. G. Nocera and Y. Shao-Horn, *J. Am. Chem. Soc.*, 2012, **134**, 16959-16962.
40. M. W. Kanan, J. Yano, Y. Surendranath, M. Dinca, V. K. Yachandra and D. G. Nocera, *J. Am. Chem. Soc.*, 2010, **132**, 13692-13701.
41. M. Risch, V. Khare, I. Zaharieva, L. Gerencser, P. Chernev and H. Dau, *J. Am. Chem. Soc.*, 2009, **131**, 6936-6937.
42. Y. Surendranath, M. W. Kanan and D. G. Nocera, *J. Am. Chem. Soc.*, 2010, **132**, 16501-16509.
43. H. Dau and I. Zaharieva, *Acc. Chem. Res.*, 2009, **42**, 1861-1870.
44. K. Takizawa, J. A. Cruz, A. Kanazawa and D. M. Kramer, *Biochim. Biophys. Acta*, 2007, **1767**, 1233-1244.
45. S. Trasatti, *Electrochim. Acta*, 1991, **36**, 225-241.
46. K. J. Laidler and M. C. King, *J. Phys. Chem.*, 1983, **87**, 2657-2664.
47. D. G. Truhlar, B. C. Garrett and S. J. Klippenstein, *J. Phys. Chem.*, 1996, **100**, 12771-12800.
48. C. Dellago, P. G. Bolhuis, F. l. S. Csajka and D. Chandler, *J. Chem. Phys.*, 1998, **108**, 1964.
49. P. Atkins and J. D. Paula, *Physical Chemistry*, W. H. Freeman and Company, United States, 2010.
50. J. N. Bronsted and W. F. K. Wynne-Jones, *J. Chem. Soc., Faraday Trans. 1*, 1928, **25**, 59-76.
51. M. G. Evans and M. Polanyi, *J. Chem. Soc., Faraday Trans. 1*, 1936, **32**, 1333-1360.
52. P. R. Wells, *Chem. Rev.*, 1963, **63**, 171-219.
53. B. Hammer and J. K. Norskov, *Impact of Surface Science on Catalysis*, Elsevier Academic Press Inc, San Diego, 2000.
54. S. G. Wang, B. Temel, J. A. Shen, G. Jones, L. C. Grabow, F. Studt, T. Bligaard, F. Abild-Pedersen, C. H. Christensen and J. K. Norskov, *Catal. Lett.*, 2011, **141**, 370-373.
55. J. Rossmeisl, A. Logadottir and J. K. Norskov, *Chem. Phys.*, 2005, **319**, 178-184.
56. M. T. M. Koper, *J. Electroanal. Chem.*, 2011, **660**, 254–260.
57. D. R. Weinberg, C. J. Gagliardi, J. F. Hull, C. F. Murphy, C. A. Kent, B. C. Westlake, A. Paul, D. H. Ess, D. G. McCafferty and T. J. Meyer, *Chem. Rev.*, 2012, **112**, 4016-4093.
58. J. K. Norskov, T. Bligaard, A. Logadottir, S. Bahn, L. B. Hansen, M. Bollinger, H. Bengaard, B. Hammer, Z. Slijivancanin, M. Mavrikakis, Y. Xu, S. Dahl and C. J. H. Jacobsen, *J. Catal.*, 2002, **209**, 275-278.
59. E. M. Fernandez, P. G. Moses, A. Toftelund, H. A. Hansen, J. I. Martinez, F. Abild-Pedersen, J. Kleis, B. Hinnemann, J. Rossmeisl, T. Bligaard and J. K. Norskov, *Angew. Chem.*, 2008, **47**, 4683-4686.
60. I. C. Man, H. Y. Su, F. Calle-Vallejo, H. A. Hansen, J. I. Martinez, N. G. Inoglu, J. Kitchin, T. F. Jaramillo, J. K. Norskov and J. Rossmeisl, *ChemCatChem*, 2011, **3**, 1159–1165.
61. J. Rossmeisl, Z. W. Qu, H. Zhu, G. J. Kroes and J. K. Norskov, *J. Electroanal. Chem.*, 2007, **607**, 83-89.
62. V. Viswanathan and H. A. Hansen, *Top. Catal.*, 2013, **57**, 215-221.
63. A. Vojvodic, F. Calle-Vallejo, W. Guo, S. Wang, A. Toftelund, F. Studt, J. I. Martinez, J. Shen, I. C. Man, J. Rossmeisl, T. Bligaard, J. K. Noorskov and F. Abild-Pedersen, *J. Chem. Phys.*, 2011, **134**, 244509.
64. B. Hammer, *Top. Catal.*, 2006, **37**, 3-16.
65. S. Trasatti, *J. Electroanal. Chem.*, 1980, **111**, 125-131.
66. J. O. Bockris and T. Otagawa, *J. Electrochem. Soc.*, 1984, **131**, 290-302.
67. J. Suntivich, K. J. May, J. B. Goodenough, H. A. Gasteiger and Y. Shao-Horn, *Science*, 2011, **334**, 1383-1385.
68. M. T. M. Koper and R. A. van Santen, *J. Electroanal. Chem.*, 1999, **472**, 126-136.
69. B. S. Mun, M. Watanabe, M. Rossi, V. Stamenkovic, N. M. Markovic and J. P. N. Ross, *J. Chem. Phys.*, 2005, **123**, 204717.
70. T. Hofmann, T. H. Yu, M. Folse, L. Weinhardt, M. Bär, Y. Zhang, B. V. Merinov, D. J. Myers, W. A. Goddard and C. Heske, *J. Phys. Chem. C*, 2012, **116**, 24016-24026.
71. F. Abild-Pedersen, A. Nilsson and J. K. Nørskov, *J. Phys. Chem. C*, 2013, **117**, 6914-6915.
72. T. H. Yu, T. Hofmann, Y. Sha, B. V. Merinov, D. J. Myers, C. Heske and W. A. Goddard, *J. Phys. Chem. C*, 2013, **117**, 26598-26607.
73. V. R. Stamenkovic, B. S. Mun, M. Arenz, K. J. J. Mayrhofer, C. A. Lucas, G. F. Wang, P. N. Ross and N. M. Markovic, *Nat. Mater.*, 2007, **6**, 241-247.
74. V. R. Stamenkovic, B. Fowler, B. S. Mun, G. F. Wang, P. N. Ross, C. A. Lucas and N. M. Markovic, *Science*, 2007, **315**, 493-497.
75. V. R. Stamenkovic, B. S. Mun, K. J. J. Mayrhofer, P. N. Ross, N. M. Markovic, J. Rossmeisl, J. Greeley and J. K. Norskov, *Angew. Chem.*, 2006, **45**, 2897-2901.
76. R. R. Adzic, J. Zhang, K. Sasaki, M. B. Vukmirovic, M. Shao, J. X. Wang, A. U. Nilekar, M. Mavrikakis, J. A. Valerio and F. Uribe, *Top. Catal.*, 2007, **46**, 249-262.
77. A. U. Nilekar, Y. Xu, J. Zhang, M. B. Vukmirovic, K. Sasaki, R. R. Adzic and M. Mavrikakis, *Top. Catal.*, 2007, **46**, 276-284.
78. J. K. Norskov, T. Bligaard, J. Rossmeisl and C. H. Christensen, *Nat. Chem.*, 2009, **1**, 37-46.
79. F. H. B. Lima, J. Zhang, M. H. Shao, K. Sasaki, M. B. Vukmirovic, E. A. Ticianelli and R. R. Adzic, *J. Phys. Chem. C*, 2007, **111**, 404-410.
80. A. Damjanovic, A. Dey and J. O. Bockris, *J. Electrochem. Soc.*, 1966, **113**, 739-746.
81. A. Damjanovic, A. Dey and J. O. Bockris, *Electrochim. Acta*, 1966, **11**, 791-814.
82. J. P. Hoare, *The Electrochemistry of Oxygen*, New York, 1968.
83. A. C. C. Tseung and S. Jasem, *Electrochim. Acta*, 1977, **22**, 31-34.
84. P. J. Ferreira, G. J. la O', Y. Shao-Horn, D. Morgan, R. Makharia, S. Kocha and H. A. Gasteiger, *J. Electrochem. Soc.*, 2005, **152**, A2256.

Energy & Environmental Science Accepted Manuscript

 This journal is © The Royal Society of Chemistry 2012

85. K. J. J. Mayrhofer, K. Hartl, V. Juhart and M. Arenz, *J. Am. Chem. Soc.*, 2009, **131**, 16348-16349.
86. M. Pourbaix, National Association of Corrosion Engineers, 1974.
87. H. A. Hansen, J. Rossmeisl and J. K. Norskov, *Phys. Chem. Chem. Phys.*, 2008, **10**, 3722-3730.
88. S. Trasatti, *Electrochim. Acta*, 2000, **45**, 2377-2385.
89. J. Zaanen, G. A. Sawatzky and J. W. Allen, *Phys. Rev. Lett.*, 1985, **55**, 418-421.
90. J. Zaanen, C. Westra and G. A. Sawatzky, *Phys. Rev. B*, 1986, **33**, 8060-8073.
91. J. B. Goodenough and J.-S. Zhou, *Chem. Mater.*, 1998, **10**, 2980-2993.
92. J. B. Torrance, P. Lacorre, C. Asavaroengchai and R. M. Metzger, *Physica C*, 1991, **182**, 351-364.
93. S. Trasatti, *Electrochim. Acta*, 1984, **29**, 1503-1512.
94. P. Ruetschi and P. Delahay, *J. Chem. Phys.*, 1955, **23**, 556.
95. J. O. Bockris and T. Otagawa, *J. Phys. Chem.*, 1983, **87**, 2960-2971.
96. M. G. Mavros, T. Tsuchimochi, T. Kowalczyk, A. McIsaac, L. P. Wang and T. V. Voorhis, *Inorg. Chem.*, 2014, **53**, 6386-6397.
97. T. A. Betley, Q. Wu, T. Van Voorhis and D. G. Nocera, *Inorg. Chem.*, 2008, **47**, 1849-1861.
98. J. B. Goodenough, R. Manoharan and M. Paranthaman, *J. Am. Chem. Soc.*, 1990, **112**, 2076-2082.
99. J. S. Noh and J. A. Schwarz, *J. Colloid Interface Sci.*, 1989, **130**, 157-164.
100. S. I. Pechenyuk, *Russ. Chem. Bull.*, 1999, **48**, 1017-1023.
101. M. Kosmulski, *J. Colloid Interface Sci.*, 2009, **337**, 439-448.
102. J. B. Goodenough and B. L. Cushing, in *Handbook of fuel cells - Fundamentals, technology and applications*, eds. W. Vielstich, H. A. Gasteiger and H. Yokokawa, Wiley, Chichester, 2003, vol. 2, pp. 520-533.
103. N. B. Halck, V. Petrykin, P. Krtil and J. Rossmeisl, *Phys. Chem. Chem. Phys.*, 2014.
104. L. A. D. Faria, J. F. C. Boodts and S. Trasatti, *J. Appl. Electrochem.*, 1996, **26**, 1195-1199.
105. M. Wohlfahrt-Mehrens and J. Heitbaum, *J. Electroanal. Chem.*, 1987, **237**, 251-260.
106. D. B. Hibbert, *J. Chem. Soc., Chem. Commun.*, 1980, 202-203.
107. J. B. Gerken, J. G. McAlpin, J. Y. Chen, M. L. Rigsby, W. H. Casey, R. D. Britt and S. S. Stahl, *J. Am. Chem. Soc.*, 2011, **133**, 14431-14442.
108. M. Haumann, C. Muller, P. Liebisch, L. Iuzzolino, J. Dittmer, M. Grabolle, T. Neisius, W. Meyer-Klaucke and H. Dau, *Biochemistry*, 2005, **44**, 1894-1908.
109. M. Haumann, P. Liebisch, C. Muller, M. Barra, M. Grabolle and H. Dau, *Science*, 2005, **310**, 1019-1021.
110. J. O. Bockris, *J. Chem. Phys.*, 1956, **24**, 817-827.
111. J. H. Zagal, F. Bedioui and J. P. Dodelet, eds., *N_4-Macrocyclic Metal Complexes*, Springer New York, 2006.
112. A. Llobet, ed., *Molecular Water Oxidation Catalysis: A Key Topic for New Sustainable Energy Conversion Schemes*, John Wiley & Sons, Ltd, 2014.
113. K. J. J. Mayrhofer, S. J. Ashton, J. Kreuzer and M. Arenz, *Int. J. Electrochem. Sci.*, 2009, **4**, 1-8.
114. K. J. J. Mayrhofer, G. K. H. Wiberg and M. Arenz, *J. Electrochem. Soc.*, 2008, **155**, P1.
115. T. J. Schmidt, H. A. Gasteiger, G. D. Stab, P. M. Urban, D. M. Kolb and R. J. Behm, *J. Electrochem. Soc.*, 1998, **145**, 2354-2358.
116. J. Suntivich, H. A. Gasteiger, N. Yabuuchi and Y. Shao-Horn, *J. Electrochem. Soc.*, 2010, **157**, B1263-B1268
117. D. S. Ginley and C. Bright, *MRS Bulletin*, 2000, **25**, 15-18.
118. F. Opekar and P. Beran, *J. Electroanal. Chem. Interfacial Electrochem.*, 1976, **69**, 1-105.
119. A. J. Bard and L. R. Faulkner, *Electrochemical Methods: Fundamentals and Applications*, Wiley, New York, 2001.
120. K. A. Stoerzinger, M. Risch, J. Suntivich, W. M. Lu, J. Zhou, M. D. Biegalski, H. M. Christen, Ariando, T. Venkatesan and Y. Shao-Horn, *Energy Environ. Sci*, 2013, **6**, 1582-1588.
121. K. R. Cooper and M. Smith, *J. Power Sources*, 2006, **160**, 1088-1095.
122. S. Trasatti and O. A. Petrii, *J. Electroanal. Chem.*, 1992, **327**, 353-376.
123. S. Brunauer, P. H. Emmett and E. Teller, *J. Am. Chem. Soc.*, 1938, **60**, 309-319.
124. S. Iseki, K. Ohashi and S. Nagaura, *Electrochim. Acta*, 1972, **17**, 2249-2265.
125. W. A. Badawy, A. G. Gad-Allah, H. A. Abd El-Rahman and M. M. Abouromia, *Surf. Coat. Technol.*, 1986, **27**, 187-196.
126. T. A. Centeno and F. Stoeckli, *J. Power Sources*, 2006, **154**, 314-320.
127. J. L. Weininger and M. W. Breiter, *J. Electrochem. Soc.*, 1963, **110**, 484-490.
128. J. L. Weininger and M. W. Breiter, *J. Electrochem. Soc.*, 1964, **111**, 707-712.
129. R. N. O'Brien and P. Seto, *J. Electroanal. Chem. Interfacial Electrochem.*, 1968, **18**, 219-230.
130. N. A. Hampson, R. J. Latham, J. B. Lee and K. I. Macdonald, *J. Electroanal. Chem. Interfacial Electrochem.*, 1971, **31**, 57-62.
131. A. Lasia and A. Rami, *J. Electroanal. Chem.*, 1990, **294**, 123-141.
132. L. Bai, L. Gao and B. E. Conway, *J. Chem. Soc., Faraday Trans.*, 1993, **89**, 235-242.
133. P. Gu, L. Bai, L. Gao, R. Brousseau and B. E. Conway, *Electrochim. Acta*, 1992, **37**, 2145-2154.
134. E. G. Gagnon, *J. Electrochem. Soc.*, 1973, **120**, 1052-1056.
135. J. Fournier, L. Brossard, J.-Y. Tilquin, R. Cote, J.-P. Dodelet, D. Guay and H. Menard, *J. Electrochem. Soc.*, 1996, **143**, 919-926.
136. G. Wu, N. Li, D.-R. Zhou, K. Mitsuo and B.-Q. Xu, *J. Solid State Chem.*, 2004, **177**, 3682-3692.
137. S. Levine and A. L. Smith, *Discussions of the Faraday Society*, 1971, **52**, 290-301.
138. C. H. Bamford and R. G. Compton, *Electrode Kinetics: Principles and Methodology*, Elsevier, New York, 1986.
139. G. Cressey, C. M. B. Henderson and G. v. d. Laan, *Phys. Chem. Miner.*, 1993, **20**, 111-119.
140. G. v. d. Laan and I. W. Kirman, *J. Phys.: Condens. Matter*, 1992, **4**, 4189-4204.

Energy & Environmental Science Accepted Manuscript

141. M. C. Biesinger, B. P. Payne, A. P. Grosvenor, L. W. M. Lau, A. R. Gerson and R. S. C. Smart, *Appl. Surf. Sci.*, 2011, **257**, 2717-2730.
142. D. R. Mullins, S. H. Overbury and D. R. Huntley, *Surf. Sci.*, 1998, **409**, 307-319.
143. R. D. Leapman, L. A. Grunes and P. L. Fejes, *Phys. Rev. B*, 1982, **26**, 614-635.
144. A. S. Andersson, B. Kalska, L. Haggstrom and J. O. Thomas, *Solid State Ionics*, 2000, **130**, 41-52.
145. O. T. Sorensen, *Thermochim. Acta*, 1976, **15**, 227-237.
146. M. Karppinen, L. Niinisto and H. Yamauchi, *J. Therm. Anal.*, 1997, **48**, 1123-1141.
147. M. Oku, J. Kimura, M. Hosoya, K. Takada and K. Hirokawa, *Fresenius. J. Anal. Chem.*, 1988, **332**, 237-241.
148. M. Karppinen, M. Matvejeff, K. Salomäki and H. Yamauchi, *J. Mater. Chem.*, 2002, **12**, 1761-1764.
149. J. B. Goodenough, *Rep. Prog. Phys.*, 2004, **67**, 1915-1993.
150. J. Zaanen and G. A. Sawatzky, *J. Solid State Chem.*, 1990, **88**, 8-27.
151. T. Arima, Y. Tokura and J. B. Torrance, *Phys. Rev. B*, 1993, **48**, 17006-17009.
152. F. M. F. de Groot, M. Grioni, J. C. Fuggle, J. Ghijsen, G. A. Sawatzky and H. Petersen, *Phys. Rev. B*, 1989, **40**, 5715-5723.
153. J. E. Huheey, E. A. Keitzer and R. L. Keiter, *Inorganic Chemistry: Principles of Structure and Reactivity*, Harper & Row, 1997.
154. F. J. Morin and T. Wolfram, *Phys. Rev. Lett.*, 1973, **30**, 1214-1217.
155. T. Wolfram and S. Ellialtioglu, *Electronic and Optical Properties of d-Band Perovskites*, Cambridge University Press, New York, 2006.
156. M. Abbate, F. M. F. Degroot, J. C. Fuggle, A. Fujimori, O. Strebel, F. Lopez, M. Domke, G. Kaindl, G. A. Sawatzky, M. Takano, Y. Takeda, H. Eisaki and S. Uchida, *Phys. Rev. B*, 1992, **46**, 4511-4519.
157. J. Suntivich, W. T. Hong, H. Nakanishi, W. Yang, J. B. Goodenough, B. Dabrowski, J. W. Freeland and Y. Shao-Horn, *J. Phys. Chem. C*, 2013, **118**, 1856-1863.
158. A. E. Bocquet, T. Mizokawa, K. Morikawa, A. Fujimori, S. R. Barman, K. Maiti, D. D. Sarma, Y. Tokura and M. Onoda, *Phys. Rev. B*, 1996, **53**, 1161-1170.
159. A. E. Bocquet, T. Mizokawa, T. Saitoh, H. Namatame and A. Fujimori, *Phys. Rev. B*, 1992, **46**, 3771-3784.
160. M. Abbate, G. Zampieri, J. Okamoto, A. Fujimori, S. Kawasaki and M. Takano, *Phys. Rev. B*, 2002, **65**.
161. M. A. Senaris-Rodriguez and J. B. Goodenough, *J. Solid State Chem.*, 1995, **118**, 323-336.
162. P. G. Radaelli and S.-W. Cheong, *Phys. Rev. B*, 2002, **66**, 094408.
163. J.-S. Zhou, J.-Q. Yan and J. B. Goodenough, *Phys. Rev. B*, 2005, **71**, 220103(R).
164. J. Suntivich, H. A. Gasteiger, N. Yabuuchi, H. Nakanishi, J. B. Goodenough and Y. Shao-Horn, *Nat. Chem.*, 2011, **3**, 546-550.
165. M. W. Haverkort, Z. Hu, J. C. Cezar, T. Burnus, H. Hartmann, M. Reuther, C. Zobel, T. Lorenz, A. Tanaka, N. B. Brookes, H. Hsieh, H.-J. Lin, C. T. Chen and L. H. Tjeng, *Phys. Rev. Lett.*, 2006, **97**, 176405.
166. Z. Hu, H. Wu, M. Haverkort, H. Hsieh, H. Lin, T. Lorenz, J. Baier, A. Reichl, I. Bonn, C. Felser, A. Tanaka, C. Chen and L. Tjeng, *Phys. Rev. Lett.*, 2004, **92**.
167. J. B. Goodenough, *J. Appl. Phys.*, 1966, **37**, 1415-&.
168. T. Wolfram and F. J. Morin, *J. Solid State Chem.*, 1975, **12**, 291-291.
169. F. Calle-Vallejo, N. G. Inoglu, H.-Y. Su, J. I. Martínez, I. C. Man, M. T. M. Koper, J. R. Kitchin and J. Rossmeisl, *Chem. Sci.*, 2013, **4**, 1245.
170. D. A. Dowden, *Catal. Rev. - Sci. Eng.*, 1971, **5**, 1-32.
171. M. Inai, C. Iwakura and H. Tamura, *Electrochim. Acta*, 1979, **24**, 993-996.
172. C. J. Ballhausen, *Introduction to Ligand Field Theory*, McGraw-Hill, New York, 1963.
173. O. G. Holmes and D. S. McClure, *J. Chem. Phys.*, 1957, **26**, 1686.
174. R. Larsson and L. Y. Johansson, *J. Power Sources*, 1990, **32**, 253-260.
175. C. Ritter, M. R. Ibarra, J. M. DeTeresa, P. A. Algarabel, C. Marquina, J. Blasco, J. Garcia, S. Oseroff and S. W. Cheong, *Phys. Rev. B*, 1997, **56**, 8902-8911.
176. A. Dinger, R. Martin, X. Mosquet, M. Rabl, D. Rizoulis, M. Russo and G. Sticher, *Batteries for Electric Cars: Challenges, Opportunities, and the Outlook to 2020*, The Boston Consulting Group, 2010.
177. J. Q. Yan, J. S. Zhou and J. B. Goodenough, *Phys. Rev. B*, 2004, **70**, 014402.
178. M. L. Medarde, *J. Phys.: Condens. Matter*, 1997, **9**, 1679-1707.
179. J. S. Zhou, J. B. Goodenough, B. Dabrowski, P. W. Klamut and Z. Bukowski, *Phys. Rev. Lett.*, 2000, **84**, 526-529.
180. J. B. Goodenough, *J. Phys. Chem. Solids*, 1958, **6**, 287.
181. M. A. Korotin, S. Y. Ezhov, I. V. Solovyev, V. I. Anisimov, D. I. Khomskii and G. A. Sawatzky, *Phys. Rev. B*, 1996, 5309-5316.
182. G. Maris, Y. Ren, V. Volotchaev, C. Zobel, T. Lorenz and T. T. M. Palstra, *Phys. Rev. B*, 2003, **67**, 224423.
183. V. Krapek, P. Novak, J. Kunes, D. Novoselov, D. M. Korotin and V. I. Anisimov, *Phys. Rev. B*, 2012, **86**, 195104.
184. D. B. Meadowcroft, *Nature*, 1970, **226**, 847-848.
185. P. M. Raccah and J. B. Goodenough, *Phys. Rev.*, 1967, **155**, 932-943.
186. T. Wolfram, E. A. Kraut and F. J. Morin, *Bull. Am. Phys. Soc.*, 1973, **18**, 335-336.
187. T. Wolfram, E. A. Kraut and F. J. Morin, *Phys. Rev. B*, 1973, **7**, 1677-1694.
188. T. Wolfram and F. J. Morin, *Appl. Phys.*, 1975, **8**, 125-141.
189. Y. Matsumoto, H. Yoneyama and H. Tamura, *Chem. Lett.*, 1975, 661-662.
190. Y. Matsumoto, H. Yoneyama and H. Tamura, *J. Electroanal. Chem.*, 1977, **83**, 237-243.
191. Y. Matsumoto, H. Yoneyama and H. Tamura, *J. Electroanal. Chem.*, 1977, **79**, 319-326.

Energy & Environmental Science Accepted Manuscript

 This journal is © The Royal Society of Chemistry 2012

192. Y. Matsumoto, H. Yoneyama and H. Tamura, *Bull. Chem. Soc. Jpn.*, 1978, **51**, 1927-1930.
193. Y. Matsumoto, J. Kurimoto and E. Sato, *J. Electroanal. Chem.*, 1979, **102**, 77-83.
194. Y. Matsumoto and E. Sato, *Electrochim. Acta*, 1979, **24**, 421-423.
195. Y. Matsumoto, H. Manabe and E. Sato, *J. Electrochem. Soc.*, 1980, **127**, 811-814.
196. Y. Matsumoto, S. Yamada, T. Nishida and E. Sato, *J. Electrochem. Soc.*, 1980, **127**, 2360-2364.
197. Y. Matsumoto and E. Sato, *Mater. Chem. Phys.*, 1986, **14**, 397-426.
198. J. B. Goodenough, *Prog. Solid State Chem.*, 1971, **5**, 145-399.
199. A. Wattiaux, J. C. Grenier, M. Pouchard and P. Hagenmuller, *J. Electrochem. Soc.*, 1987, **134**, 1714-1718.
200. A. Wattiaux, J. C. Grenier, M. Pouchard and P. Hagenmuller, *J. Electrochem. Soc.*, 1987, **134**, 1718-1724.
201. R. G. Egdell, J. B. Goodenough, A. Hamnett and C. Naish, *J. Chem. Soc., Faraday Trans. 1*, 1983, **79**, 893-912.
202. Y. Lee, J. Kleis, J. Rossmeisl, Y. Shao-Horn and D. Morgan, *Energy Environ. Sci*, 2011, **4**, 3966-3970.
203. A. Fujimori, *J. Phys. Chem. Solids*, 1992, **53**, 1595-1602.
204. E. Antolini, J. R. C. Salgado and E. R. Gonzalez, *J. Power Sources*, 2006, **160**, 957-968.
205. G. A. Parks, *Chem. Rev.*, 1965, **65**, 177-198.
206. E. McCafferty and J. P. Wightman, *J. Colloid Interface Sci.*, 1997, **194**, 344-355.
207. M. Lazzeri and A. Selloni, *Phys. Rev. Lett.*, 2001, **87**, 266105.
208. R. Pentcheva, F. Wendler, H. L. Meyerheim, W. Moritz, N. Jedrecy and M. Scheffler, *Phys. Rev. Lett.*, 2005, **94**, 126101.
209. R. J. Francis, S. C. Moss and A. J. Jacobson, *Phys. Rev. B*, 2001, **64**, 235425.
210. K. J. May, C. E. Carlton, K. A. Stoerzinger, M. Risch, J. Suntivich, Y.-L. Lee, A. Grimaud and Y. Shao-Horn, *J. Phys. Chem. Lett.*, 2012, **3**, 3264-3270.
211. L. D. Burke, O. J. Murphy, J. F. Oneill and S. Venkatesan, *J. Chem. Soc., Faraday Trans. 1*, 1977, **73**, 1659-1671.
212. R. Frydendal, E. A. Paoli, B. P. Knudsen, B. Wickman, P. Malacrida, I. E. L. Stephens and I. Chorkendorff, *ChemElectroChem*, 2014, **1**, 2075-2081.
213. S. H. Chang, N. Danilovic, K. C. Chang, R. Subbaraman, A. P. Paulikas, D. D. Fong, M. J. Highland, P. M. Baldo, V. R. Stamenkovic, J. W. Freeland, J. A. Eastman and N. M. Markovic, *Nat. Commun.*, 2014, **5**, 4191.
214. V. M. Goldschmidt, *Naturwissenschaften*, 1926, **14**, 477-485.
215. S. Svarcova, K. Wiik, J. Tolchard, H. J. M. Bouwmeester and T. Grande, *Solid State Ionics*, 2008, **178**, 1787-1791.
216. J. I. Jung, H. Y. Jeong, J. S. Lee, M. G. Kim and J. Cho, *Angew. Chem.*, 2014.
217. Y. L. Lee, J. Kleis, J. Rossmeisl and D. Morgan, *Phys. Rev. B*, 2009, **80**.
218. K. P. Yao, Y. C. Lu, C. V. Amanchukwu, D. G. Kwabi, M. Risch, J. Zhou, A. Grimaud, P. T. Hammond, F. Barde and Y. Shao-Horn, *Phys. Chem. Chem. Phys.*, 2014, **16**, 2297-2304.
219. J. Mannhart and D. G. Schlom, *Science*, 2010, **327**, 1607-1611.
220. E. Dagotto, *Science*, 2007, **318**, 1076-1077.
221. A. Sawa, A. Yamamoto, H. Yamada, T. Fujii, M. Kawasaki, J. Matsuno and Y. Tokura, *Appl. Phys. Lett.*, 2007, **90**, 252102.
222. Y. Miyahara, K. Miyazaki, T. Fukutsuka and T. Abe, *J. Electrochem. Soc.*, 2014, **161**, F694-F697.
223. M. Sase, F. Hermes, K. Yashiro, K. Sato, J. Mizusaki, T. Kawada, N. Sakai and H. Yokokawa, *J. Electrochem. Soc.*, 2008, **155**, B793.
224. E. J. Crumlin, E. Mutoro, S. J. Ahn, G. J. la O, D. N. Leonard, A. Borisevich, M. D. Biegalski, H. M. Christen and Y. Shao-Horn, *J. Phys. Chem. Lett.*, 2010, **1**, 3149-3155.
225. M. E. Lynch, L. Yang, W. Qin, J.-J. Choi, M. Liu, K. Blinn and M. Liu, *Energy Environ. Sci*, 2011, **4**, 2249.
226. H. Ding, A. V. Virkar, M. Liu and F. Liu, *Phys. Chem. Chem. Phys.*, 2013, **15**, 489-496.
227. Z. Feng, E. J. Crumlin, W. T. Hong, D. Lee, E. Mutoro, M. D. Biegalski, H. Zhou, H. Bluhm, H. M. Christen and Y. Shao-Horn, *J. Phys. Chem. Lett.*, 2013, **4**, 1512-1518.
228. M. Komo, A. Hagiwara, S. Taminato, M. Hirayama and R. Kanno, *Electrochemistry*, 2012, **80**, 834-838.
229. D. Fuchs, C. Pinta, T. Schwarz, P. Schweiss, P. Nagel, S. Schuppler, R. Schneider, M. Merz, G. Roth and H. v. Löhneysen, *Phys. Rev. B*, 2007, **75**.
230. W. S. Choi, J. H. Kwon, H. Jeen, J. E. Hamann-Borrero, A. Radi, S. Macke, R. Sutarto, F. He, G. A. Sawatzky, V. Hinkov, M. Kim and H. N. Lee, *Nano Lett.*, 2012, **12**, 4966-4970.
231. W. T. Hong, M. Gadre, Y.-L. Lee, M. D. Biegalski, H. M. Christen, D. Morgan and Y. Shao-Horn, *J. Phys. Chem. Lett.*, 2013, **4**, 2493-2499.
232. Z. Feng, Y. Yacoby, W. T. Hong, H. Zhou, M. D. Biegalski, H. M. Christen and Y. Shao-Horn, *Energy Environ. Sci*, 2014, **7**, 1166.
233. Y. Yacoby, H. Zhou, R. Pindak and I. Božović, *Phys. Rev. B*, 2013, **87**.
234. J. Guzman and B. C. Gates, *J. Am. Chem. Soc.*, 2004, **126**, 2672-2673.
235. P.-A. Carlsson, L. Osterlund, P. Thormahlen, A. Palmqvist, E. Fridell, J. Jansson and M. Skoglundh, *J. Catal.*, 2004, **226**, 422-434.
236. X. Liu, A. Wang, T. Zhang, C.-Y. Mou and J.-F. Lee, *J. Catal.*, 2011, **278**, 288-296.
237. J. Guzman and B. C. Gates, *J. Phys. Chem. B*, 2002, **106**, 7659-7665.
238. R. Zanella, S. Giorgio, C.-H. Shin, C. R. Henry and C. Louis, *J. Catal.*, 2004, **222**, 357-367.
239. Y. Yuan, K. Asakura, H. Wan, K. Tsai and Y. Iwasawa, *Catal. Lett.*, 1996, **42**, 15-20.
240. J. Guzman, S. Carrettin and A. Corma, *J. Am. Chem. Soc.*, 2005, **127**, 3286-3287.
241. Y. Nagai, T. Yamamoto, T. Tanaka, S. Yoshida, T. Nonaka, T. Okamoto, A. Suda and M. Sugiura, *Catal. Today*, 2002, **74**, 225-234.
242. T. Tanaka, H. Yamashita, R. Tsuchitani, T. Funabiki and S. Yoshida, *J. Chem. Soc., Faraday Trans. 1*, 1988, **84**, 2987-2999.

Energy & Environmental Science Accepted Manuscript

243. M. Risch, A. Grimaud, K. J. May, K. A. Stoerzinger, T. J. Chen, A. N. Mansour and Y. Shao-Horn, *J. Phys. Chem. C*, 2013, **117**, 8628-8635.
244. F. Tao, M. E. Grass, Y. Zhang, D. R. Butcher, F. Aksoy, S. Aloni, V. Altoe, S. Alayoglu, J. R. Renzas, C.-K. Tsung, Z. Zhu, Z. Liu, M. Salmeron and G. A. Somorjai, *J. Am. Chem. Soc.*, 2010, **132**, 8697-8703.
245. F. Tao, M. E. Grass, Y. Zhang, D. R. Butcher, J. R. Renzas, Z. Liu, J. Y. Chung, B. S. Mun, M. Salmeron and G. A. Somorjai, *Science*, 2008, **322**, 932-934.
246. H. Bluhm, K. Andersson, T. Araki, K. Benzerara, G. E. Brown, J. J. Dynes, S. Ghosal, M. K. Gilles, H. C. Hansen, J. C. Hemminger, A. P. Hitchcock, G. Ketteler, A. L. D. Kilcoyne, E. Kneedler, J. R. Lawrence, G. G. Leppard, J. Majzlam, B. S. Mun, S. C. B. Myneni, A. Nilsson, H. Ogasawara, D. F. Ogletree, K. Pecher, M. Salmeron, D. K. Shuh, B. Tonner, T. Tyliszczak, T. Warwick and T. H. Yoon, *J. Electron Spectrosc. Relat. Phenom.*, 2006, **150**, 86-104.
247. D. F. Ogletree, H. Bluhm, G. Lebedev, C. S. Fadley, Z. Hussain and M. Salmeron, *Rev. Sci. Instrum.*, 2002, **73**, 3872.
248. M. E. Grass, P. G. Karlsson, F. Aksoy, M. Lundqvist, B. Wannberg, B. S. Mun, Z. Hussain and Z. Liu, *Rev. Sci. Instrum.*, 2010, **81**, 053106.
249. T. Schiros, L.-A. Naslund, K. Andersson, J. Gyllenpalm, G. S. Karlberg, M. Odelius, H. Ogasawara, L. G. M. Pettersson and A. Nilsson, *J. Phys. Chem. C*, 2007, **111**, 15003.
250. T. Schiros, O. Takahashi, K. J. Andersson, H. Ostrom, L. G. Pettersson, A. Nilsson and H. Ogasawara, *J. Chem. Phys.*, 2010, **132**, 094701.
251. D. J. Miller, H. Oberg, S. Kaya, H. Sanchez Casalongue, D. Friebel, T. Anniyev, H. Ogasawara, H. Bluhm, L. G. Pettersson and A. NIlsson, *Phys. Rev. Lett.*, 2011, **107**, 195502.
252. H. Bluhm, *J. Electron Spectrosc. Relat. Phenom.*, 2010, **177**, 71-84.
253. S. Yamamoto, T. Kendelewicz, J. T. Newberg, G. Ketteler, D. E. Starr, E. R. Mysak, K. J. Andersson, H. Ogasawara, H. Bluhm, M. Salmeron, J. G. E. Brown and A. Nilsson, *J. Phys. Chem. C*, 2010, **114**, 2256-2266.
254. J. T. Newberg, D. E. Starr, S. Yamamoto, S. Kaya, T. Kendelewicz, E. R. Mysak, S. Porsgaard, M. B. Salmeron, J. G. E. Brown, A. Nilsson and H. Bluhm, *J. Phys. Chem. C*, 2011, **115**, 12864-12872.
255. Z. Nagy and H. You, *Electrochim. Acta*, 2002, **47**, 3037-3055.
256. R. Feidenhans'l, *Surf. Sci. Rep.*, 1989, **10**, 105-188.
257. I. K. Robinson and D. J. Tweet, *Rep. Prog. Phys.*, 1992, **55**, 599-651.
258. A. Nakahara, M. Nakamura, K. Sumitani, O. Sakata and N. Hoshi, *Langmuir*, 2007, **23**, 10879-10882.
259. C. A. Lucas, N. M. Markovic and P. N. Ross, *Surf. Sci.*, 1995, **340**, L949-L954.
260. T. Kondo, J. Morita, K. Hanaoka, S. Takakusagi, K. Tamura, M. Takahasi, J. Mizuki and K. Uosaki, *J. Phys. Chem. C*, 2007, **111**, 13197-13204.
261. P. J. Eng, *Science*, 2000, **288**, 1029-1033.
262. M. Sowwan, Y. Yacoby, J. Pitney, R. MacHarrie, M. Hong, J. Cross, D. Walko, R. Clarke, R. Pindak and E. Stern, *Phys. Rev. B*, 2002, **66**.
263. Y. Yacoby, M. Sowwan, E. Stern, J. O. Cross, D. Brewe, R. Pindak, J. Pitney, E. M. Dufresne and R. Clarke, *Nat. Mater.*, 2002, **1**, 99-101.
264. Z. Feng, Y. Yacoby, M. J. Gadre, Y.-L. Lee, W. T. Hong, H. Zhou, M. D. Biegalski, H. M. Christen, S. B. Adler, D. Morgan and Y. Shao-Horn, *J. Phys. Chem. Lett.*, 2014, **5**, 1027-1034.
265. H. Zhou, Y. Yacoby, V. Y. Butko, G. Logvenov, I. Bozovic and R. Pindak, *Proc. Natl. Acad. Sci. U. S. A.*, 2010, **107**, 8103-8107.
266. R. Herger, P. Willmott, C. Schlepütz, M. Björck, S. Pauli, D. Martoccia, B. Patterson, D. Kumah, R. Clarke, Y. Yacoby and M. Döbeli, *Phys. Rev. B*, 2008, **77**.
267. B. B. Nelson-Cheeseman, H. Zhou, P. V. Balachandran, G. Fabbris, J. Hoffman, D. Haskel, J. M. Rondinelli and A. Bhattacharya, *Adv. Funct. Mater.*, 2014, DOI: 10.1002/adfm.201401077.

Energy & Environmental Science Accepted Manuscript

 This journal is © The Royal Society of Chemistry 2012